

EVALUATION OF RANS-BASED TURBULENCE MODELS FOR ISOTHERMAL FLOW IN A REALISTIC CAN-TYPE GAS TURBINE COMBUSTOR APPLICATION

Aishvarya Kumar¹, Ram Prakash Bharti^{a,*}

^a*Complex Fluid Dynamics and Microfluidics (CFDM) Lab, Department of Chemical Engineering, Indian Institute of Technology Roorkee, Roorkee - 247667, Uttarakhand, INDIA*

Abstract

In the present study, RANS-based turbulence models are assessed to simulate the isothermal flow in a combustor representing a constituent can combustor of the can-annular configuration used in jet engines. The models assessed are two equation models: standard k-epsilon, realizable k-epsilon, standard k-omega, SST k-omega and Linear Pressure Strain Reynolds Stress Model. The models were assessed by comparing their predictions of mean axial velocity, mean transverse velocity, turbulent kinetic energy and shear stress to experimental data at two different positions in the combustor: the primary holes plane and the dilution holes plane. The comparison showed that the two-equation models failed to predict the confined swirling flow accurately at both positions. The realizable k-epsilon model was the least accurate, followed by the standard k-epsilon model. The standard K-omega performed slightly better, while the SST K-omega model was the most accurate among the two-equation models. The discrepancies between the predicted and experimental results could be attributed to the isotropic turbulence assumptions which are invalid for confined swirling flows and two-equation models also lack formulations to capture the intricacies of vortex flow and its interaction with the surrounding flows in confined swirling flows. The Linear Pressure Strain RSM model, which considers turbulence anisotropy, showed some promise, although overpredicted, results were in trend with experimental values at the primary holes plane. However, at the dilution holes plane, the model overpredicted the velocity field i.e. mean axial velocity and underestimated the turbulence field including turbulent kinetic energy and shear stress. These observed discrepancies can be ascribed to the pressure-strain correlation in the Linear Pressure Strain RMS model which assumes the pressure-strain correlation is a linear function of the strain-rate tensor. However, for complex flows, this linear assumption is too simplistic. Hence, the results of this study suggest that more advanced turbulence models are needed to accurately predict the confined swirling flow in combustors.

Keywords: RANS, turbulence, gas turbine combustor, jet engine combustor, combustor aerodynamics, confined swirling flows, Reynolds Stress Model

1. INTRODUCTION

The history of gas turbine engines goes back to the 1920s with the initial work of British Scientist Sir Frank Whittle, who first patented the concept in 1930 (Leyes and Fleming, 1999). His design used a compressor to increase the pressure of incoming air, which was mixed with fuel and then ignited to form high-velocity gases that drove a turbine which provided the thrust to move the aircraft. This rotating turbine provided the thrust to move the aircraft and also, in turn, powered the compressor. During the World War II. gas turbine (or jet) engines (jet engines) were primarily used in military aircraft, subsequently, their potential for civil aviation was recognized with the de Havilland Comet becoming the world's first commercial airliner, powered by four Rolls Royce Avon turbojet engines (Royce, 2015). Since then, gas turbines have become a prominent power source for commercial and military aircraft as well as for a wide range of applications like power generation and marine propulsion. Advances in technology have led to enhancement in efficiency, lower emissions and higher reliability that have made gas turbines vital for the modern transport and power generation industry. However, with advancements in technology, the principle of operation remains the same for modern gas turbines as those of invented ones.

Gas turbine engines have several primary components (such as compressor, combustor, turbine, and exhaust) that work together to produce the power to propel aircraft, generate electricity or provide mechanical power. These components include the compressor which is the first component, it takes air from the atmosphere and compresses it, increasing the air pressure and temperature. The compressed air is then supplied to the combustor. The combustor is where the fuel is injected into the compressed air and ignited, producing high-temperature high pressure which is directed towards the turbine. The turbine is driven by the high-pressure and

* *Corresponding author.*

Email address: rpbharti@iitr.ac.in (Ram Prakash Bharti)

¹Independent Researcher; Former Researcher, Department of Engineering, City University of London, UK

high-temperature gas from the combustion chamber. The turbine and compressor are assembled on the same shaft, hence, the energy extracted from the gas also drives the compressor and other components like fans (in turbofan jets), generators or even propellers (in the case of turboprop aircraft). The exhaust is the final stage of the gas turbine engine, the hot gas from the turbine is directed out of the engine through the nozzle, producing thrust in the aircraft or when used for power generation the exhaust gas is used in a heat recovery system to capture the remaining heat energy. Thus, the combustor being an essential component of gas turbine engines, its design plays a crucial role in determining the engine's performance, efficiency and emissions. The combustor is responsible for mixing fuel and igniting the mixture to produce high-temperature and pressure gas. An ideal, well-designed combustor ensures complete combustion of the fuel-air mixture, resulting in high combustion efficiency, improved engine performance, and reduced emissions. A good combustor must be designed for high temperatures and pressures, as well as harsh operating conditions (e.g., high temperature, high pressure) of gas turbine engines. They must be designed to minimize issues like flameout and flashback that can occur during combustion (Lefebvre and Ballal, 2010).

There are three main types of combustor geometries used in gas turbine engines, each having its own merits. Can combustor: In this type of system, individual combustion chambers (cans) are located along the engine's diameter. The can-type combustors were first used in aircraft engines in the 1940s and 1950s (Lefebvre and Ballal, 2010; Carter, 1946). The second type of combustor used in gas turbine engines is Can-annular or tubo-annular. In this system, several combustor cans are arranged in a ring or annulus and cans are connected by interconnecting channels (Lefebvre and Ballal, 2010). Examples include Rolls Royce Spey (Gradon and Miller, 1968a), Rolls Royce Marine Spey (Gradon and Miller, 1968b), and Pratt and Whitney JT8D (Hall and Chapman, 1964). The third type of combustor chamber design is the annular type. It consists of a ring-shaped combustion chamber that surrounds a turbine shaft. The annular type design allows more complete and efficient combustion, resulting in improved

fuel efficiency and lower emissions. Being more compact and having fewer components, the annular design also reduced weight. It is widely used in modern gas turbine engines, particularly suitable for large commercial aircraft examples include General Electric CF6-50 and the Rolls Royce RB211 (Lefebvre and Ballal, 2010). The main parts of combustors are the combustor liner which is often made from porous walls, fuel injector, igniter, swirler, primary holes, dilution holes, discharge or exhaust nozzle and combustor liner. The combustor liner is the key component of the combustor, it is part of the combustor that forms the walls of the combustion chamber and contains the hot, high-pressure gases produced by the combustion. The liner must withstand the high temperature and pressures of the combustion process, well as the corrosive effects of the hot gases and possible impurities in the fuel. The combustor liner geometry can have a significant impact on the performance of the gas turbine engine. The typical combustor liner geometry has mainly three main sub-geometries: dome, barrel, and nozzle. The primary region of the combustor has dome, injector, swirler, and primary holes are the parts of the primary region of the combustor. Swirlers are employed to create swirling motion in the fuel-air mixture, which helps improves mixing and achieves complete combustion and lower emissions. Collectively dome geometry of the combustor liner, swirler geometry, fuel injector geometry and placement of the primary holes and their size strongly affect the fuel-air mixing process in the primary region of the combustor thus the overall performance of the combustor making the combustor aerodynamics a highly vital field of study for combustor design. The combustor aerodynamics also assist in the placement of dilution holes that are meant to provide cooler air into the combustor which helps in the even distribution of air-fuel mixture throughout the combustor and even assists in reaching the complete combustion state alongside preventing the development of hot spots that could damage the combustor liner. The reduction in the overall temperature in the combustor also helps in reducing the production of NO_x during the combustion. The exhaust nozzle accelerates the exhaust gas up to high velocity and low pressure and directs it to the turbine (Lefebvre and Ballal, 2010). Hence, the shape and

size of the exhaust nozzle of the combustor play a significant role in gas turbine engine performance, and therefore also requires a thorough aerodynamic study to be optimised.

2. LITERATURE REVIEW

Hence, many isothermal studies have been performed to enhance the understanding of combustor aerodynamics before combustion flow analysis. The LDV (Laser Doppler Anemometry) technique has often been employed to measure the velocity fields like Mean and fluctuating components. Research on realistic models includes studies performed at Imperial College London on the combustor can representing the geometry of the Rolls Royce Spey gas turbine engine at different operating conditions (Heitor and Whitelaw, 1986). The combustor was made from a porous material Transply and the working fluid was air. Velocity measurements indicated that the vortical structure in the primary zone is predominantly influenced by the swirler flow, with a partial contribution from the primary jets. The strongly swirling flow was evident from the depression of the profile in the reverse flow region and positive velocities near the axis. The mean swirl velocity profiles demonstrated relatively high values in the primary zone, further amplified in the secondary holes plane due to the effective reduction of the swirling core diameter. The swirl velocity's strength decreased in the exit plane, although the swirl was still present. The LDV studies have also been performed on transparent perspex water combustor (Koutmos and McGuirk, 1989) models by the same research group on similar geometry/conditions (Heitor and Whitelaw, 1986) The transparent model provided them with optical access to visualise the development of vortical structures by injecting dye in the combustor and also hydrogen bubbles in the combustor. The velocity profiles obtained were in line with those obtained using the Transply combustor, the die displayed the presence of a vortical structure originating due to swirl motion in the primary zone and reaching the combustor exit. The hydrogen bubbles showed the development of a toroidal vortex upstream

of the axis of the primary holes. [Bicen et al. \(1989\)](#) performed Following, a series of experimental studies were conducted on the modified geometry with enlarged Dilution Holes representing the Rolls Royce Tay combustor geometry were performed ([Bicen et al., 1989](#)). Through observation, it was noted that jets were formed by water entering the combustor through six primary holes that penetrated almost radially. These jets collided at the centerline, feeding the development of a toroidal recirculation zone in the head of the combustor. The impingement of the primary jets created a strong backflow that transported the swirler flow close to the combustor wall and the primary jets until it reached the dilution plane of dilution jets. Additionally, a small recirculation region was formed near the combustor head (dome) as a result of the swirler flow. Observations also showed that since dilution holes were more staggered because of having a larger diameter, dilution jets blocked the upstream swirler fluid near and wall and forced it to mix with the central core formed by the primary jet impingement. Regions of high anisotropy were found at the central core where the tangential turbulence intensity was recorded twice the axial turbulence intensity. Their further research ([McGuirk and Palma, 1995](#)) substantiated the above-mentioned.

Acknowledging the significance of understanding the aerodynamics of the combustor during the non-reactive stage and the potential of CFD for optimising its design and improving its performance, numerous isothermal CFD studies have been conducted. Early numerical simulation investigations ([Srinivasan and Mongia, 1980](#); [Sturgess and Syed, 1990](#); [Sloan et al., 1986](#); [Nallasamy, 1987](#); [Xia et al., 1998](#)) performed on confined swirling flows representing idealized axis-symmetrical can combustors using the standard k-epsilon model showed the inadequacy of standard $k - \epsilon$ model to predict such flows with adverse pressure gradient accurately owing to the isotropic eddy viscosity formulation. On realistic geometry, [Koutmos and McGuirk \(1991\)](#) conducted numerical simulations of isothermal flow in a practical single can combustor representing an individual can combustor of the can-annular Rolls Royce Spey engine combustors, using the standard k-epsilon model. LDV (Laser-Doppler Velocimetry)

measurements were used to validate the accuracy of the simulations which showed moderately good agreements at primary and intermediate zones, however, discrepancies increased in the dilution region. Results also showed that the standard k-epsilon model predicted levels of turbulence energy are too low in regions of high anisotropy. Following, [McGuirk and Palma \(1993\)](#) evaluated the accuracy of the standard k-epsilon model in predicting the behavior of a practical single can combustor representing an individual can combustor of the turbo-annular Rolls Royce Tay engine combustors. They validated their simulation results using LDV measurements and found that the largest discrepancies between the measured and predicted values were in the primary region of the combustor. The model exhibited higher levels of momentum diffusion than measurement, and the turbulence level was again underpredicted in the primary jet impingement region, which is a highly anisotropic area. On realistic geometry, numerical simulations were performed ([Koutmos and McGuirk, 1991](#); [McGuirk and Palma, 1993](#)) to evaluate the accuracy of the standard $k - \epsilon$ model in predicting the isothermal flow in a practical single can-annular combustor representing an individual can of can-annular Rolls Royce Spey engine ([Koutmos and McGuirk, 1991](#)) and the turbo-annular Rolls Royce Tay engine ([McGuirk and Palma, 1993](#)). The Tay combustor differed from the Spey combustor by having larger dilution holes. Compared with LDV measurements, the simulation results showed moderately good agreement at primary and intermediate zones; however, discrepancies increased in the dilution region ([Koutmos and McGuirk, 1991](#)) and the largest discrepancies in the primary region of the combustor ([McGuirk and Palma, 1993](#)). The model exhibited higher levels of momentum diffusion and underpredicted turbulence energy in the primary jet impingement, a high anisotropy region.

Researchers have attempted to use the turbulence models with a second-order closure method for simulating confined swirling flows. For instance, [Jones and Pascau \(1989\)](#) performed simulations for swirling confined flows using the standard k-epsilon model and RSM. Comparison with experimental results showed the superiority of RSM over standard $k - \epsilon$, in

comparison with experimental results, for swirling confined flows,. The researchers noted that the standard k -epsilon model did not incorporate any methodology to consider the stabilizing effects of swirling motion, which resulted in notable differences between the predicted and measured mean velocity fields. [Weber et al. \(1990\)](#) found in their investigation that isotropic turbulent viscosity formulation in the standard $k - \epsilon$ model's isotropic turbulent viscosity formulation was inadequate in predicting flows with adverse pressure gradients in confined swirling flow applications. RSM model provided more accurate predictions. [Lai \(1996\)](#) compared the accuracy of standard k -epsilon, RNG k -epsilon, and RSM models in simulating swirling confined flow. They found RSM to be the most accurate model, while RNG $k - \epsilon$ was less accurate than standard $k - \epsilon$, particularly at a swirl number of 0.5. [Xia et al. \(1998\)](#) also compared standard $k - \epsilon$, RNG $k - \epsilon$, and Reynolds Stress models in predicting swirling flow in a water model combustion chamber. Reynolds Stress predicted the results most accurately, while the other models predicted solid-body rotation type flow downstream. [German and Mahmud \(2005\)](#) numerical investigation of the industrial-grade combustor model also showed RSM model predicted flow more accurately than the standard $k - \epsilon$ model. Their prediction also showed RSM model accurately predicted that the internal recirculation zone extended to the combustor exit, while the standard $k - \epsilon$ model failed to do so. [Jawarneh and Vatistas \(2006\)](#) also showed that RSM is effective in predicting swirling flow characteristics.

High Fidelity Simulations techniques such as Large Eddy Simulation (LES) have also been applied to model isothermal swirling confined flows. [Jones et al. \(2012\)](#) performed non-reacting Large Eddy Simulations of the idealized model axis-symmetric combustor with sudden expansion. Their comparison with experimental data showed that they achieved fairly good accuracy and were able to reproduce the macro features of the confined swirling flows accurately such as Precessing Vortex Core (PVC). Recent studies ([Palkin et al., 2022](#); [Wang et al., 2022](#)) used LES to simulate isothermal flow in a square combustion chamber, finding good agreement with experimental data but noting a small discrepancy due to insufficient grid

resolution in the shear layer. [Palkin et al. \(2022\)](#) performed LES simulation results for isothermal flows in a square combustion chamber that agreed with experimental PIV data, similar to [Wang et al. \(2022\)](#). However, it can be argued that none of the above-mentioned high-fidelity simulation reference cases had essential features of real combustors like primary holes, dilution holes, and exit nozzle. Hence, the results cannot be extrapolated for realistic geometries.

The present study focuses on developing sound strategies for the accurate prediction of swirling flow at non-reacting conditions in a realistic gas turbine combustor at a lower computational cost. This paper strives to enrich the understanding of the research community of modeling swirling flows in gas turbine combustors through accurate prediction and thorough analysis of the flow field at the non-reacting conditions. The authors believe that the methodology developed in the present research will also help researchers to simulate reacting flow accurately. The ultimate aim of this study is to provide engineers and designers of various fields from aeronautics to power plants and microturbines with cost-effective strategies for achieving optimal combustor design in less computational time. The authors chose the RANS modeling approach due to its efficient and accurate prediction capabilities for the target flows while also being relatively less computationally expensive and time-consuming.

In particular, this study assesses and compares the predictive ability of various RANS models like standard $k - \epsilon$ ([Launder and Spalding, 1972](#)), realizable $k - \epsilon$ ([Shih et al., 1995](#)), standard $k - \omega$ ([Wilcox, 1998](#)), SST $k - \omega$ ([Menter, 1994](#)) and Linear Pressure Strain Reynolds Stress Model (LPS-RSM) ([Gibson and Launder, 1978](#); [Fu et al., 1987](#); [Launder, 1989](#)) to predict the swirl flow in combustor geometry. The reference case is from experimental studies of ([Heitor and Whitelaw, 1986](#); [Heitor, 1985](#)) under non-reacting conditions as the reference case. The combustor geometry represents an individual can of the turbo-annular Rolls Royce Spey engine combustor. The steady flow conditions were acknowledged before LDV measurements. To the authors' knowledge, this is the first novel study to investigate this in the considered

geometry. The evaluation of the models is performed by comparing the predicted results with the experimental Laser Doppler Velocimetry (LDV) data for mean velocity, turbulent kinetic energy, and shear stress.

3. FLOW CONFIGURATION

The combustor chamber is shown in Fig. 1 used in experimental investigations was a model of the tubo-annular or can-annular combustor representative of the Rolls–Royce Spey gas turbine. The combustor model (Fig. 1) included a hemispherical head, a cylindrical barrel, and a circular to rectangular nozzle.

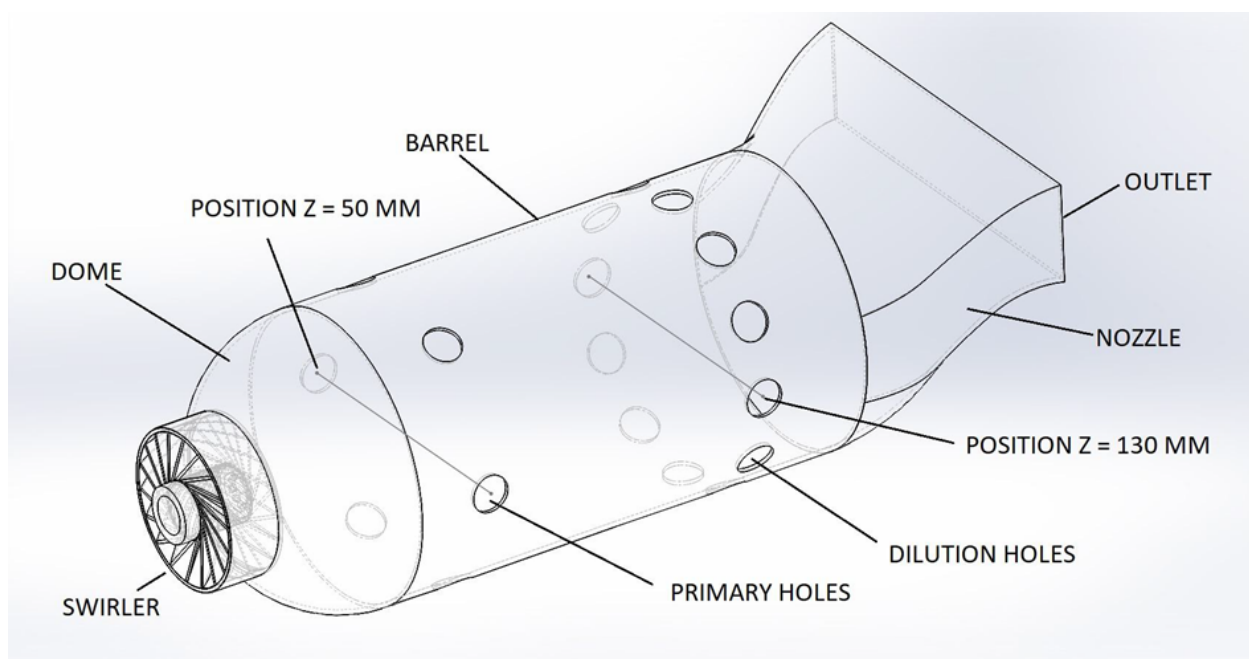


Figure 1: Combustor geometry with the positions for velocity measurement.

3.1. Reference Case Experimental Setup and Conditions (Heitor and Whitelaw, 1986; Heitor, 1985)

The details of the experimental setup and conditions are as follows. Two rows of primary and dilution holes were located in the combustor barrel, with six primary and twelve dilution holes. The walls of the combustor walls were constructed using Transply, which is a laminated porous material designed by Rolls-Royce plc. The combustor featured a curved vane swirler located on the head, consisting of 18 vanes oriented at 45° with a maximum thickness of 0.56 mm. The combustor had a fuel injector located at the centre of the swirler, which was in the shape of a 90° cone with 10 equally spaced 1.7 mm diameter holes located on a 4.50 mm radius through which fuel is injected into the chamber. In this setup, the combustor was situated within a sizeable duct, and the primary and dilution jets enter the combustor at an angle of approximately 90° to its axis.

For isothermal flow conditions, air, instead of propane, was injected into the combustor through the injector with the same mass flow rate as propane (1.63 g/s), implying the average velocity of air through each hole was 49 m/s. The bulk flow velocity (U_b) is recorded as 31 m/s (Heitor and Whitelaw, 1986; Heitor, 1985). The atmospheric pressure was 1 atm and the room temperature was around 318K during the experimental studies. The positions on the primary holes $z = 50$ mm and dilution holes axis $z = 130$ mm where LDV measurements were taken are illustrated in Fig. 1.

As per the report, of the total mass airflow of 0.085 kg/s, 7% of the air went into the combustor through the dome section, 14% of the air went into the combustor through the barrel wall section and 6% of the air went into the combustor through the nozzle wall section. Therefore,

Table 1: Experimental conditions at isothermal run.

Air flow rate (combustor) (g/s)	Air flow rate (injector nozzle) (g/s)	P_0 (atm)	Temperature (K)
85	1.63	1	318

Table 2: Boundary Conditions for CFD Simulation - Isothermal Run.

Boundary	Swirler	Primary Holes	Dilution Holes	Dome	Barrel	Nozzle
Air flow (%)	24	16	33	7	14	6
Air flow (g/s)	20.4	2.2667×6	2.3375×12	5.95	11.9	5.1

these walls are modelled as mass flow inlet boundary conditions in the present study. Around 24% of air entered into the injector through a swirler, 16% of the air went into the injector through primary holes and 33% of the air went into the injector through dilution holes. The experimental conditions are listed in Table 1 and boundary conditions are listed in Table 2. The combustor geometry and experimental details are described in greater detail in (Heitor and Whitelaw, 1986; Heitor, 1985). A schematic representation of the combustor is shown in Fig. 1.

4. METHODOLOGY

The mathematical model for the problem under consideration is written as follows.

4.1. Governing Equations

Steady-state incompressible RANS (Reynolds-Averaged Navier-Stokes) equations (Versteeg and Malalasekera, 2007; Alfonsi, 2009) have been employed and have the following form:

$$\frac{\partial \bar{u}_i}{\partial x_i} = 0 \quad (1)$$

$$\rho \frac{\partial \bar{u}_i}{\partial t} + \rho \bar{u}_j \frac{\partial \bar{u}_i}{\partial x_j} = \rho \bar{f}_i + \frac{\partial}{\partial x_i} [-\bar{p} \delta_{ij} + 2\mu \bar{S}_{ij} - \rho \overline{u'_i u'_j}] \quad (2)$$

$$\bar{S}_{ij} = \frac{1}{2} \left[\frac{\partial \bar{u}_i}{\partial x_j} + \frac{\partial \bar{u}_j}{\partial x_i} \right] \quad (3)$$

Where \bar{S}_{ij} is the mean rate of the strain tensor, \bar{u}_i is the mean fluid velocity in i^{th} direction, ρ is the density of the fluid, \bar{p} is the mean pressure, μ is the dynamics viscosity, \bar{f}_i is the source term for body forces like gravity, δ_{ij} is Kronecker delta and is 1 when $i = j$ and 0 when $i \neq j$, and

$(-\rho \overline{u'_i u'_j})$ is the apparent stress owing to the fluctuating velocity field and is generally referred to as Reynolds stress.

In this study, the Reynolds stress $(-\rho \overline{u'_i u'_j})$ for two-equation models is modelled using Boussinesq's approximation, which is defined below. which can be shorthand as

$$-\rho \overline{u'_i u'_j} = 2\mu_t [\overline{S}_{ij}] - \frac{2}{3}\rho k \delta_{ij} \quad (4)$$

Where k is the turbulent kinetic energy is defined by the following equation

$$k = \frac{1}{2} \left[(\overline{u'_i})^2 + (\overline{u'_j})^2 + (\overline{u'_k})^2 \right] \quad (5)$$

As above mentioned, the constant temperature was maintained in the test rig in the experimental study, therefore, the process is considered isothermal and hence energy equation is not used. The derivations of the above equations can be found in (Versteeg and Malalasekera, 2007; Alfonsi, 2009).

4.2. Turbulence Models

The turbulence models, such as standard $k - \epsilon$, realizable $k - \epsilon$, standard $k - \omega$, SST $k - \omega$, and Linear Pressure Strain - Reynolds Stress Model (LPS-RSM), used in this study are expressed as follows.

4.2.1. Standard $k - \epsilon$ model

In the standard $\kappa - \epsilon$ model (Launder and Spalding, 1972), the transport equations of turbulent kinetic energy (k), and turbulent dissipation rate (ϵ) is obtained from the following equations:

are as follows.

$$\frac{\partial \rho k}{\partial t} + \frac{\partial}{\partial x_j} (\rho k \bar{u}_j) = \frac{\partial}{\partial x_j} \left[\left(\mu + \frac{\mu_t}{\sigma_k} \right) \frac{\partial k}{\partial x_j} \right] + 2\mu_t \bar{S}_{ij} \cdot \bar{S}_{ij} - \rho \epsilon \quad (6)$$

$$\frac{\partial \rho \epsilon}{\partial t} + \frac{\partial}{\partial x_j} (\rho \epsilon \bar{u}_j) = \frac{\partial}{\partial x_j} \left[\left(\mu + \frac{\mu_t}{\sigma_\epsilon} \right) \frac{\partial \epsilon}{\partial x_j} \right] + C_{1\epsilon} \frac{\epsilon}{k} 2\mu_t \bar{S}_{ij} \cdot \bar{S}_{ij} - C_{2\epsilon} \frac{\epsilon^2}{k} + S_\epsilon \quad (7)$$

where k is the turbulent kinetic energy, μ_t is the turbulent (or eddy) viscosity assumed to be isotropic, ϵ is the turbulence dissipation rate, and is defined by the following term are defined as follows.

$$\epsilon = 2\nu \overline{s'_{ij} s'_{ij}} \quad (8)$$

$$\mu_t = \rho C_\mu \frac{k^2}{\epsilon} \quad (9)$$

where C_μ is a constant. The model constants ($C_{1\epsilon}$, $C_{2\epsilon}$, C_μ , σ_k , σ_ϵ) have the following values.

$$C_{1\epsilon} = 1.44, \quad C_{2\epsilon} = 1.92, \quad C_\mu = 0.09, \quad \sigma_k = 1.0, \quad \sigma_\epsilon = 1.3$$

These values have been experimentally determined (Launder and Spalding, 1972) for fundamental turbulent flows, including frequently encountered shear flows like boundary layers, mixing layers, and jets, as well as for decaying isotropic grid turbulence.

4.2.2. Realizable $k - \epsilon$ model

In the realizable $k - \epsilon$ model, the transport equation for turbulence kinetic energy (k) remains same (i.e., Eq. 6) as the standard $k - \epsilon$ model; however, the transport equation of turbulent dissipation rate (ϵ) is derived using the transport equation of mean square of vorticity fluctuation (Tennekes and Lumley, 2018). The realizable $k - \epsilon$ model (Shih et al., 1995), the turbulent kinetic energy (k) and turbulent dissipation rate (ϵ) are obtained from the following

equations are written as follows:

$$\frac{\partial \rho k}{\partial t} + \frac{\partial}{\partial x_j} (\rho k \bar{u}_j) = \frac{\partial}{\partial x_j} \left[\left(\mu + \frac{\mu_t}{\sigma_k} \right) \frac{\partial k}{\partial x_j} \right] + 2\mu_t \bar{S}_{ij} \cdot \bar{S}_{ij} - \rho \epsilon \quad (10)$$

$$\frac{\partial \rho \epsilon}{\partial t} + \frac{\partial}{\partial x_j} (\rho \epsilon \bar{u}_j) = \frac{\partial}{\partial x_j} \left[\left(\mu + \frac{\mu_t}{\sigma_\epsilon} \right) \frac{\partial \epsilon}{\partial x_j} \right] + \rho C_1 S \epsilon - \rho C_2 \frac{\epsilon^2}{k + \sqrt{\nu \epsilon}} \quad (11)$$

where $C_1 = \max \left(0.43, \frac{\eta}{\eta + 5} \right)$, $\eta = S \left(\frac{k}{\epsilon} \right)$, $S = \sqrt{2 \bar{S}_{ij} \cdot \bar{S}_{ij}}$

$$C_2 = 1.9, \quad C_{1\epsilon} = 1.44, \quad \sigma_k = 1, \quad \sigma_\epsilon = 1.2$$

where, k is the turbulent kinetic energy, ϵ is the turbulence dissipation rate and, and μ_t is the turbulent viscosity or eddy viscosity and is defined by the following term which is similarly to the standard $k - \epsilon$ model by Eqs. (8) and (9), respectively. The eddy viscosity in the realizable $k - \epsilon$ model is also assumed to be isotropic and is computed using the following equation similar to the standard $k - \epsilon$ model: To be realizable, the model requires maintaining non-negativity of normal stress ($\overline{u_i'^2} \geq 0$) and ‘‘Schwarz inequality’’ (Heitor, 1985; Launder and Spalding, 1972). The Schwarz inequality is defined by the following term.

$$\overline{u_i'^2} \geq 0 \quad \text{and} \quad \frac{(\overline{u_i' u_j'})^2}{\overline{u_i'^2} \overline{u_j'^2}} \leq 1 \quad (12)$$

Schwarz inequality binds the magnitude of shear stress in a fluid and ensures that the stresses are realistic and physically meaningful. The turbulence velocity formulation remains isotropic. The realizability of the model is achieved by modifying C_μ in Eq. (9), which is constant in the standard $k - \epsilon$ model, by introducing the additional terms and coefficients that depend on the strain and rotation rates of the flows and aimed to assist in improving the turbulence-predicting

ability, as follows.

$$C_\mu = \frac{1}{A_0 + A_s(kU^*/\epsilon)} \quad (13)$$

$$\text{here } U^* \equiv \sqrt{\bar{S}_{ij} \cdot \bar{S}_{ij} + \tilde{\Omega}_{ij} \tilde{\Omega}_{ij}} \quad (14)$$

$$\text{and } \tilde{\Omega}_{ij} = \bar{\Omega}_{ij} - \nabla \times \omega_k, \quad \bar{\Omega}_{ij} = \frac{1}{2} \left[\frac{\partial \bar{u}_i}{\partial \bar{x}_j} - \frac{\partial \bar{u}_j}{\partial \bar{x}_i} \right] \quad (15)$$

where $\bar{\Omega}_{ij}$ is the mean rate of rotation tensor, viewed in a moving reference frame with angular velocity (ω_k). The model constant A_0 and A_s are given as

$$A_0 = 4.04, \quad A_s = \sqrt{6} \cos \phi, \quad \phi = \frac{1}{3} \cos^{-1}(\sqrt{6}W), \quad W = \frac{\bar{S}_{ij} \bar{S}_{jk} \bar{S}_{ki}}{\bar{S}^3}, \quad \tilde{S} = \sqrt{\bar{S}_{ij} \bar{S}_{ij}}$$

These terms are aimed to assist in improving the turbulence-predicting ability of the model.

4.2.3. Standard $k - \omega$ model

The turbulent kinetic energy k , and specific dissipation rate $\omega = \epsilon/k$, which is a ratio of ϵ to k , are obtained from the following equation in the standard $k - \omega$ model (Wilcox, 1998).

$$\frac{\partial \rho k}{\partial t} + \frac{\partial}{\partial x_j} (\rho k \bar{u}_j) = \frac{\partial}{\partial x_j} \left[\left(\mu + \frac{\mu_t}{\sigma_k} \right) \frac{\partial k}{\partial x_j} \right] + 2\mu_t \bar{S}_{ij} \cdot \bar{S}_{ij} - \rho \beta^* f_{\beta^*} k \omega \quad (16)$$

$$\frac{\partial \rho \omega}{\partial t} + \frac{\partial}{\partial x_j} (\rho \omega \bar{u}_j) = \frac{\partial}{\partial x_j} \left[\left(\mu + \frac{\mu_t}{\sigma_\omega} \right) \frac{\partial \omega}{\partial x_j} \right] + \alpha \left(\frac{\omega}{k} \right) 2\mu_t \bar{S}_{ij} \cdot \bar{S}_{ij} - \rho \beta f_\beta \omega^2 \quad (17)$$

where, $\sigma_k = 2.0$, and $\sigma_\omega = 2.0$. The isotropic eddy viscosity (μ_t) is computed from the following equation:

$$\mu_t = \alpha^* \frac{\rho k}{\omega} \quad (18)$$

(a) *Low Reynolds number correction:* The coefficient α^* (in Eq. 18) damps the turbulent viscosity causing a low Reynolds number (Re) correction given by:

$$\alpha^* = \alpha_\infty^* \left(\frac{\alpha_0^* + Re_k}{1 + Re_k} \right) \quad (19)$$

where $Re_k = \frac{Re_t}{R_k}$, $Re_t = \frac{\rho k}{\mu_t \omega}$, $R_k = 6$, $\alpha_o^* = \frac{\beta_i}{3}$, $\beta_i = 0.072$, $\alpha_\infty^* = 1$

In the high Reynolds number form of the $k - \omega$ model, $\alpha^* = \alpha_\infty^* = 1$.

(b) *Production of ω :* In the production term $\alpha(\omega/k)2\mu_t\bar{S}_{ij} \cdot \bar{S}_{ij}$ in Eq. (17), the coefficient α in the production term ($\alpha(\omega/k)2\mu_t\bar{S}_{ij} \cdot \bar{S}_{ij}$) in Eq. (17), is given by

$$\alpha = \frac{\alpha_\infty}{\alpha^*} \left(\frac{\alpha_0 + Re_\omega}{1 + Re_\omega} \right), \quad Re_\omega = \frac{Re_t}{R_\omega}, \quad R_\omega = 2.95, \quad \alpha_\infty = 0.52, \quad \alpha_0 = \frac{1}{9} \quad (20)$$

where $Re_\omega = (Re_t/R_\omega)$, $R_\omega = 2.95$, α^* and Re_t are given by Eq. (19). In the high Reynolds number form of the $k - \omega$ model, $\alpha^* = \alpha_\infty^* = 1$.

(c) *Modelling turbulence dissipation:* The factors (f_{β^*} , β^* , f_β and β) in the dissipation terms ($\rho\beta^*f_{\beta^*}k\omega$, and $\rho\beta f_\beta\omega^2$) of the transport equation of k in Eqs. (16) and (17) are given by

$$f_{\beta^*} = \begin{cases} 1 & \chi_k \leq 0 \\ (1 + 680\chi_k^2)/(1 + 400\chi_k^2) & \chi_k > 0 \end{cases}, \quad f_\beta = \frac{1 + 70\chi_\beta}{1 + 80\chi_\beta} \quad (21)$$

$$\beta^* = \beta_i^* [1 + \zeta^* F(M_t)], \quad \beta = \beta_i \left[1 - \frac{\beta_i^*}{\beta_i} \zeta^* F(M_t) \right] \quad (22)$$

where $\beta_i^* = \beta_\infty^* \left[\frac{(4/15) + (Re_\beta)^4}{1 + (Re_\beta)^4} \right]$, $Re_\beta = \frac{Re_t}{R_\beta}$, $R_\beta = 8$, $\zeta^* = 1.5$, $\beta_\infty^* = 0.09$

$$\chi_k \equiv \frac{1}{\omega^3} \frac{\partial k}{\partial x_j} \frac{\partial \omega}{\partial x_j}, \quad \chi_\beta = \left| \frac{\Omega_{ij}\Omega_{jk}S_{ki}}{(\beta_\infty^*\omega)^3} \right|$$

$$\Omega_{ij} = \frac{1}{2} \left[\frac{\partial u_i}{\partial x_j} - \frac{\partial u_j}{\partial x_i} \right], \quad S_{ki} = \frac{1}{2} \left[\frac{\partial u_i}{\partial x_k} + \frac{\partial u_k}{\partial x_i} \right]$$

In the dissipation term $\rho\beta f_\beta\omega^2$ of the transport equation of ω in Eq. (17) *(d) Compressibility correction*: $F(M_t)$ is a compressibility function $F(M_t)$ appearing in Eq. (22) is given by

$$F(M_t) = \begin{cases} 0 & M_t < M_{t0} \\ M_t^2 - M_{t0}^2 & M_t > M_{t0} \end{cases} \quad (23)$$

$$\text{where } M_t^2 \equiv \frac{2k}{a^2}, \quad M_{t0} = 0.25, \quad a = \sqrt{\gamma RT} \quad (24)$$

where γ is the adiabatic index, R is the gas constant, a is the speed of sound, and T is the temperature.

In the high Reynolds number form of the $k - \omega$ model, $\beta_i^* = \beta_\infty^*$, and $\alpha^* = \alpha_\infty^* = 1$. In the incompressible form, $\beta^* = \beta_i^*$. The model constants are as follows:

4.2.4. Shear stress transport (SST) $k - \omega$ model

The SST shear stress transport $k - \omega$ model (Menter, 1994) effectively blends the formulation of $k - \omega$ model in the near-wall region and $k - \epsilon$ model in the outer region of the flow. The turbulent kinetic energy (k) and specific dissipation rate (ω) are obtained from the following equation:

$$\frac{\partial \rho k}{\partial t} + \frac{\partial}{\partial x_j} (\rho k \bar{u}_j) = \frac{\partial}{\partial x_j} \left[\left(\mu + \frac{\mu_t}{\sigma_k} \right) \frac{\partial k}{\partial x_j} \right] + 2\mu_t \bar{S}_{ij} \cdot \bar{S}_{ij} - \rho \beta^* f_{\beta^*} k \omega \quad (25)$$

$$\frac{\partial \rho \omega}{\partial t} + \frac{\partial}{\partial x_j} (\rho \omega \bar{u}_j) = \frac{\partial}{\partial x_j} \left[\left(\mu + \frac{\mu_t}{\sigma_\omega} \right) \frac{\partial \omega}{\partial x_j} \right] + \left(\frac{\alpha}{\nu_t} \right) 2\mu_t \bar{S}_{ij} \cdot \bar{S}_{ij} - \rho \beta_i f_\beta k \omega^2 + D_\omega \quad (26)$$

The isotropic eddy viscosity is computed from the following equation:

$$\text{where, } \mu_t = \frac{\rho k}{\omega} \left(\max \left[\frac{1}{\alpha^*}, \frac{S_{ij} F_2}{\alpha_1 \omega} \right] \right)^{-1}, \quad (27)$$

$$\sigma_k = \left(\frac{F_1}{\sigma_{k,1}} + \frac{1 - F_1}{\sigma_{k,2}} \right)^{-1}, \quad \sigma_\omega = \left(\frac{F_1}{\sigma_{\omega,1}} + \frac{1 - F_1}{\sigma_{\omega,2}} \right)^{-1} \quad (28)$$

$$F_1 = \tanh(\phi_1^4), \quad F_2 = \tanh(\phi_2^2) \quad (29)$$

$$\phi_1 = \min \left[\max(g_1, g_2), \frac{4\rho k}{\sigma_{\omega,2} D_\omega^+ y^2} \right], \quad \phi_2 = \max(2g_1, g_2)$$

$$g_1 = \frac{\sqrt{k}}{0.09\omega y}, \quad g_2 = \frac{500\mu}{\rho y^2 \omega}, \quad D_\omega^+ = \max \left[2\rho \frac{1}{\rho_{\omega,2}} \frac{1}{\omega} \frac{\partial k}{\partial x_j} \frac{\partial \omega}{\partial x_j}, 10^{-10} \right]$$

Where α^* is defined in Eq. (19), F_1 and F_2 are blending functions, y is the distance to the next surface, and D_ω^+ is the positive portion of the cross-diffusion term (D_ω).

(a) *Modelling turbulence production:* The turbulence production term $2\mu_t \bar{S}_{ij} \cdot \bar{S}_{ij}$ in Eq. (25) represents the production of k is the same as the standard $k - \omega$ model. The term $(\alpha/\nu_t) 2\mu_t \bar{S}_{ij} \cdot \bar{S}_{ij}$ found (in Eq. 26) represents the production of ω , α is given by Eq. (20) with α_∞ is given by

$$\alpha_\infty = [F_1 \alpha_{\infty,1} + (1 - F_1) \alpha_{\infty,2}] \quad (30)$$

$$\text{where, } \alpha_{\infty,j} = \left(\frac{\beta_{i,j}}{\beta_\infty^*} - \frac{\kappa^2}{\sigma_{\omega,j} \sqrt{\beta_\infty^*}} \right), \quad \kappa = 0.41$$

(b) *Modelling turbulence dissipation:* The dissipation of k in the SST $k - \omega$ model is defined similarly as in the standard $k - \omega$ model using the term $\rho \beta^* k \omega$ in Eq. (25). In the SST K-omega model f_{β^*} is constant and is equal to 1. The dissipation of ω in the SST $k - \omega$ model is also defined in a similar way as in the standard $k - \omega$ model using the term $\rho \beta_i \omega^2$ in Eq. (26). The f_β is constant and is equal to 1. The β_i is given by the following equation

$$\beta_i = F_1 \beta_{i,1} + (1 - F_1) \beta_{i,2} \quad (31)$$

where, F_1 is obtained from Eq. (29).

(c) *Cross diffusion modification:* The SST $k - \omega$ model is based on both the standard $k - \omega$ model

and the standard $k - \epsilon$ model. To blend these two models, the standard $k - \epsilon$ model is transformed into equations based on the $k - \omega$ model which leads to the introduction of a cross-diffusion term defined by the following term in the Eq. (26).

$$D_\omega = 2(1 - F_1) \rho \frac{1}{\omega \sigma_{\omega,2}} \frac{\partial k}{\partial x_j} \frac{\partial \omega}{\partial x_j} \quad (32)$$

(d) *Model constants:* The model constants are as follows: $\sigma_{k,1} = 1.176$, $\sigma_{\omega,1} = 2.0$, $\sigma_{k,2} = 1.0$, $\sigma_{\omega,2} = 1.168$, $a_1 = 0.31$, $\beta_{i,1} = 0.075$, $\beta_{i,2} = 0.0828$. All other model constants (i.e., α_∞^* , α_∞ , α_0 , β_∞^* , R_β , R_k , R_ω , ζ^* , M_{t0}) in SST $k - \omega$ model have the same values as the standard $k - \omega$ model.

4.2.5. Linear Pressure Strain - Reynolds Stress Model (LPS-RSM)

Abandoning the isotropic eddy viscosity hypothesis, the RSM closes the RANS equations by solving the transport equation of Reynolds stresses ($R_{11}, R_{22}, R_{33}, R_{12}, R_{13}, R_{23}$) alongside the equation for the dissipation rate. Thus, for the 3D flow, seven additional equations are required to be solved for the 3D flow addition to the mean flow equations (i.e., continuity and momentum equations) must be solved.

Reynolds Stress equation models are based on the utilization of Reynolds Stress Transport Equations. The transport equation for the transport of Reynolds stresses $R_{ij} = \overline{u'_i u'_j}$.

$$\begin{aligned} \underbrace{\frac{\partial}{\partial t} (\rho R_{ij})}_{\text{local time derivative}} + \underbrace{\frac{\partial}{\partial x_k} (\rho u_k R_{ij})}_{C_{ij} \equiv \text{Convection term}} &= - \underbrace{\frac{\partial}{\partial x_k} \left[\overline{\rho u'_i u'_j u'_k} + \overline{p' (\delta_{kj} u'_i + \delta_{ik} u'_j)} \right]}_{D_{T,ij} \equiv \text{Turbulent Diffusion}} \\ + \underbrace{\frac{\partial}{\partial x_k} \left[\mu \frac{\partial}{\partial x_k} (\overline{u'_i u'_j}) \right]}_{D_{M,ij} \equiv \text{Molecular Diffusion}} - \underbrace{\rho \left(\overline{u'_i u'_k} \frac{\partial u_j}{\partial x_k} + \overline{u'_j u'_k} \frac{\partial u_i}{\partial x_k} \right)}_{P_{ij} \equiv \text{Stress Production}} \\ + \underbrace{p' \left(\frac{\partial \overline{u'_i}}{\partial x_j} + \frac{\partial \overline{u'_j}}{\partial x_i} \right)}_{\phi_{ij} \equiv \text{Pressure Strain}} - \underbrace{2\mu \frac{\partial \overline{u'_i}}{\partial x_k} \frac{\partial \overline{u'_j}}{\partial x_k}}_{\epsilon_{ij} \equiv \text{Dissipation}} \end{aligned} \quad (33)$$

In Eq. (33), while the terms $D_{M,ij}$ and P_{ij} require no extra modelling. While the other three terms $D_{T,ij}$, ϕ_{ij} and ϵ_{ij} need to be modelled to close the equation. The turbulent diffusion term ($D_{T,ij}$) is modelled using the following equation

$$D_{T,ij} = \frac{\partial}{\partial x_k} \left(\frac{\mu_t}{\sigma_k} \frac{\partial \overline{u'_i u'_j}}{\partial x_k} \right) \quad (34)$$

where, $\sigma_k = 0.82$ (Lien and Leschziner, 1994). The turbulent viscosity (μ_t) is computed using Eq. (9). The tensor (ϵ_{ij}) is modelled using

$$\epsilon_{ij} = \rho \epsilon \frac{2}{3} \delta_{ij} \left(1 + 2 \frac{k}{a^2} \right) \quad (35)$$

where a is the speed of sound (Eq. 24), the scalar dissipation rate ϵ is computed using an equation similar to that used in the standard $k-\epsilon$ model (Eq. 8), and turbulent kinetic energy (k) is obtained by taking the trace of Reynolds stress tensor.

$$k = \frac{1}{2} \overline{u'_i u'_i} \quad (36)$$

In this study, the Linear Pressure Strain Reynolds Stress Model (LPS-RSM) is employed that models the pressure strain term (ϕ_{ij}), its formulation is based on the proposal of (Gibson and Launder, 1978; Fu et al., 1987; Launder, 1989). The model uses the following decomposition to model (ϕ_{ij}) into the slow pressure strain ($\phi_{ij,1}$), rapid pressure strain ($\phi_{ij,2}$), and wall reflection strain ($\phi_{ij,w}$) as follows.

$$\phi_{ij} = \phi_{ij,1} + \phi_{ij,2} + \phi_{ij,w} \quad (37)$$

where $\phi_{ij,1}$ is called the slow pressure strain term, $\phi_{ij,2}$ is known as rapid pressure strain term and $\phi_{ij,w}$ is called the wall reflection term. The slow pressure term ($\phi_{ij,1}$) is modelled as where $C_1 = 1.8$. The slow pressure strain term ($\phi_{ij,1}$) can also be represented using the Reynolds stress

anisotropy tensor (b_{ij}) as

$$\phi_{ij,1} = -2C_1\rho\epsilon b_{ij} \quad \text{where} \quad C_1 = 1.8, \quad b_{ij} = -\frac{1}{2k} \left(-\overline{u'_i u'_i} + \frac{2}{3}\delta_{ij}k \right) \quad (38)$$

The rapid pressure strain term ($\phi_{ij,2}$) is modelled as

$$\phi_{ij,2} = -C_2 \left[(P_{ij} - C_{ij}) - \frac{2}{3}\delta_{ij} \left(\frac{1}{2}P_{kk} - \frac{1}{2}C_{kk} \right) \right] \quad \text{where} \quad C_2 = 0.60 \quad (39)$$

where $C_2 = 0.60$, P_{ij} and C_{ij} are defined in Eq. (33).

The wall reflection term ($\phi_{ij,w}$) redistributes normal stress near the wall. It tends to dampen the normal stress perpendicular to the wall while enhancing the stresses parallel to the wall. The term is modelled as

$$\begin{aligned} \phi_{ij,w} \equiv & C'_1 \frac{\epsilon}{k} \left(\overline{u'_k u'_m} n_k n_m \delta_{ij} - \frac{3}{2} \overline{u'_i u'_k} n_j n_k - \frac{3}{2} \overline{u'_j u'_k} n_i n_k \right) \frac{C_l k^{\frac{3}{2}}}{\epsilon d} \\ & + C'_2 \left(\phi_{km,2} n_k n_m \delta_{ij} - \frac{3}{2} \phi_{ik,2} n_j n_k - \frac{3}{2} \phi_{jk,2} n_i n_k \right) \frac{C_l k^{\frac{3}{2}}}{\epsilon d} \end{aligned} \quad (40)$$

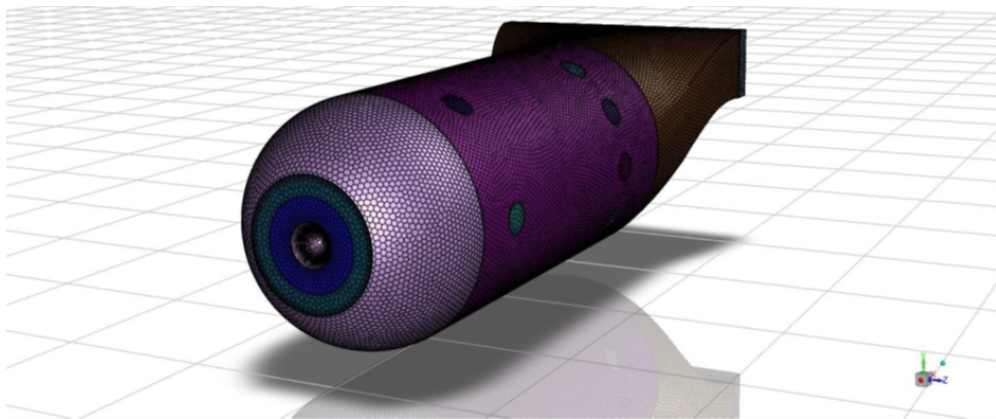
where $C'_1 = 0.5$, $C'_2 = 0.3$, $C_l = (C_\mu^{\frac{3}{4}}/\kappa)$, $C_\mu = 0.09$, n_k is the x_k component of the unit normal to the wall, d is the normal distance to the wall, and $\kappa = 0.4187$ is the von Karman constant.

5. NUMERICAL APPROACH

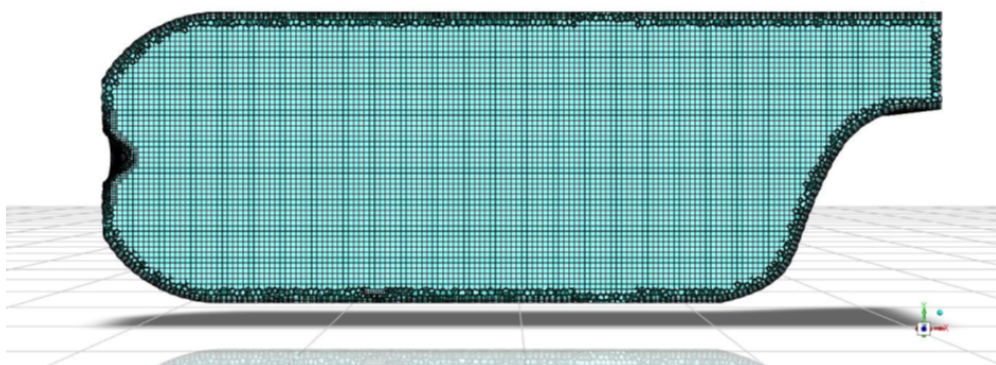
In this study, the governing equations are solved using the ANSYS Fluent 2022 R1 (student version) solver, which employs the finite volume method (Versteeg and Malalasekera, 2007). Given the quasi-steady nature of the flow regime (Heitor and Whitelaw, 1986), the steady-state simulations have been conducted. The pressure-velocity coupling was achieved through the utilization of a coupled algorithm (Ghobadian and Vasquez, 2007). The discretization of mass and momentum employed the second-order upwind scheme, while the PRESTO scheme (Patankar, 1980), which is specifically recommended for swirling flow (Cellek and Pinarbasi, 2018), was used to discretize the pressure.

The mesh generation is also performed using ANSYS Fluent 2022 R1 Student version. The mesh type is poly-hexacore, a hybrid type of mesh containing a hexahedral core and polyhedral outer shell (see Fig. 2). Three layers of polyhedral prism-type cells on the walls have been generated to capture the boundary layer well (see Fig. 2(b)). The swirler effective area is computed using the approach proposed by [McGuirk and Palma \(1992\)](#), and the boundary conditions (Table 2) are modeled using the approach proposed by [Crocker et al. \(1997\)](#), similar to previous studies conducted by ([Jones, 2002](#); [di Mare et al., 2004](#); [Oefelein, 2006](#); [Veynante, 2009](#)).

In the mesh convergence study, the influence of grid density on velocity and turbulence fields is assessed. Mesh Convergence simulations are performed using the standard $k - \epsilon$ model



(a) Front view



(b) A sectional view

Figure 2: Schematics of the mesh.

(Launder and Spalding, 1972). The simulation of near-wall turbulence was conducted is simulated using the enhanced wall treatment Method (EWT). EWT is a modeling approach that combines linear (i.e., laminar) and logarithmic (i.e., turbulent) laws of the wall using a joining function (Kader, 1981). Following the guidelines (Celik et al., 2008), the ratio $r = h_{\text{coarse}}/h_{\text{fine}}$ of Max cell length is maintained above 1.3 (Celik et al., 2008). The characteristics of the meshes used in this study are described in Table 3. The boundary conditions used are described in Table 2.

Table 3: Mesh characteristics.

Mesh	Elements	Maximum cell length, h (m)	$r = h_{\text{coarse}}/h_{\text{fine}}$
1	113599	0.003	–
2	210417	0.00225	1.333
3	429720	0.0016	1.40625

6. RESULTS AND DISCUSSION

Before presenting the assessment of the turbulence model in predicting the isothermal flow in a realistic can-type gas turbine combustor geometry (refer Fig. 1), the mesh independence study has first been performed and discussed. Subsequently, the reliability and accuracy of the present modeling approach are presented by comparing and validating the present predictions with the limited experimental results available in the literature (Heitor and Whitelaw, 1986; Heitor, 1985). The velocity field is normalized using the bulk velocity ($U_b = 31$ m/s) (Heitor and Whitelaw, 1986; Heitor, 1985) and radial position is normalized by the internal radius ($R_c = 37.5$ mm) as $r^* = r/R_c$.

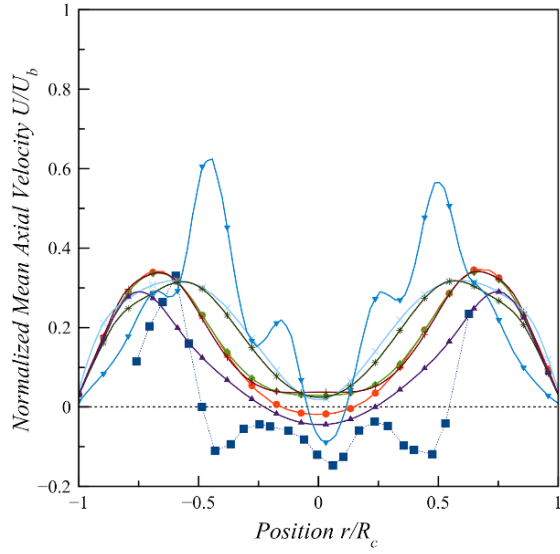
6.1. Mesh independence study

The predicted velocity and turbulence characteristics obtained using the three different grids (Table 2) and standard $k - \epsilon$ model are compared in Figs. 3 and 4. The predicted velocity profiles

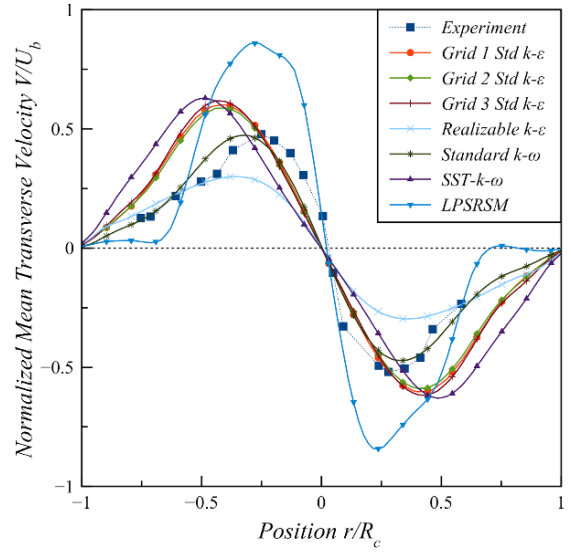
are normalized using the bulk velocity which is $U_b = 31$ m/s (Heitor and Whitelaw, 1986; Heitor, 1985). The predicted axial velocity (U/U_b) profiles at the position $z = 50$ mm (on the primary holes plane) in Fig. 3(a) on grids 1, 2, and 3 show similarity. However, while observing the predicted mean axial velocity profile prediction of grid 1, it can be seen that it is reaching a negative value at the radial position $r/R_c = -0.25$ to 0.25 . This is mainly attributed to the lower density of mesh elements in grid 1 which has resulted in numerical diffusion errors (Versteeg and Malalasekera, 2007). Furthermore, in Fig. 3(b), the transverse velocity predictions at the position $z = 50$ mm indicate minimal variations for grids 1, 2, and 3.

On observing the predicted Turbulent kinetic energy (k) for the same position ($z = 50$ mm) on primary holes plane, predicted results in Fig. 3(c) show a steeper profile for obtained using a dense grid than the course grid. However, it can be stated that variations between grids 1, 2 and 3 are not immense. This is because as the mesh element size becomes smaller, the magnitude of the mean velocity gradient increases with refinement in the mesh (i.e., decreasing mesh element size), resulting in the observed variation. This behavior has also previously been observed in the author's previous research (Kumar, 2017; Kumar et al., 2021a,b). The same trend can be seen for the shear stress in Fig. 3(d), as the magnitude of the computed shear stress depends directly on the magnitude of mean velocity gradients in two-equation models (see Eq. 3).

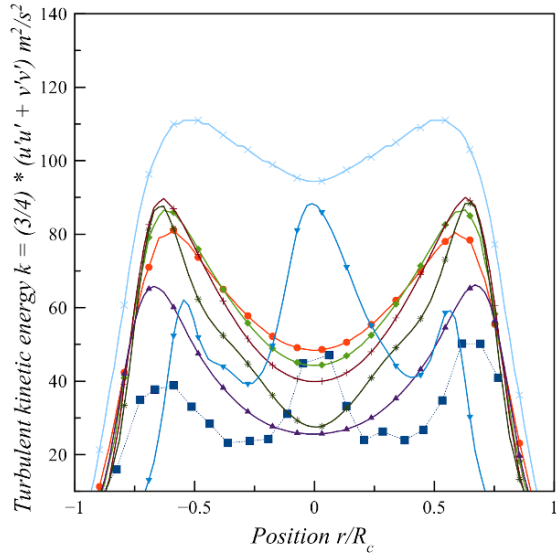
Subsequently, the influence of mesh size on the predicted velocity and turbulence characteristics at the position $z = 130$ mm (on the dilution holes plane) are analyzed and shown in Fig. 4. While observing the predicted axial velocity at the position $z = 130$ mm (on the dilution holes plane) in Fig. 4(a), it is apparent that predictions using grids 1, 2 and 3 are similar. The presence of numerical diffusion is less pronounced at $z = 130$ mm compared to at $z = 50$ mm, where the swirling motion was highly dominant. The mean transverse velocity profile on the same position, as shown in Fig. 4(b) also suggests similar profiles obtained for grids 1, 2 and 3. The mean transverse velocity profiles using the standard $k - \epsilon$ model also



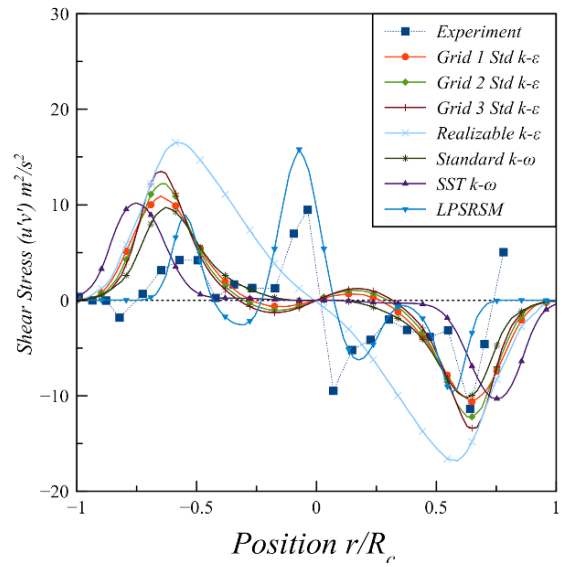
(a) Axial Velocity



(b) Transverse Velocity



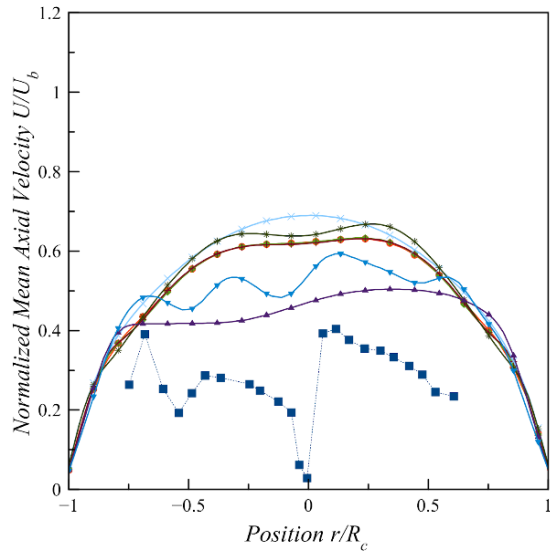
(c) Turbulent Kinetic Energy



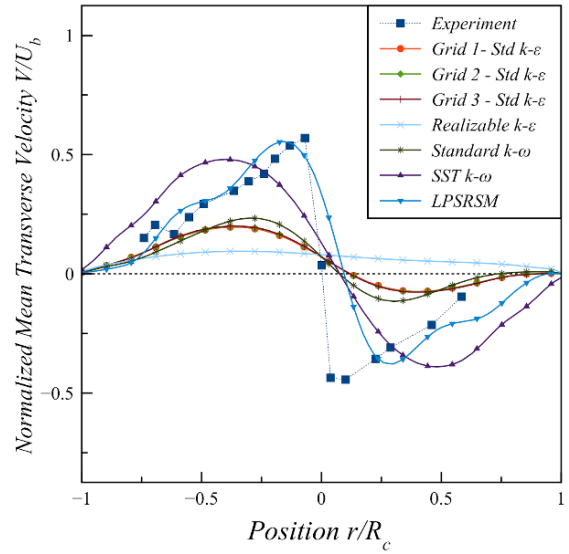
(d) Shear Stress

Figure 3: Velocity and turbulence characteristics at axial position $z = 50$ mm on primary holes plane at isothermal flow conditions.

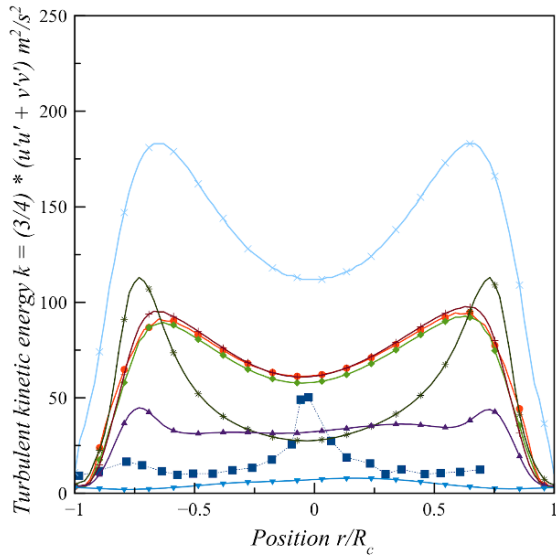
indicates diffusion of the swirl as the flow convects to the dilution holes using the used turbulence model. Further, the predicted turbulent kinetic energy (k) the shear stress profiles show a similar trend at $z = 130$ mm in Figs. 4(c) and Fig. 4(d) as observed for the position



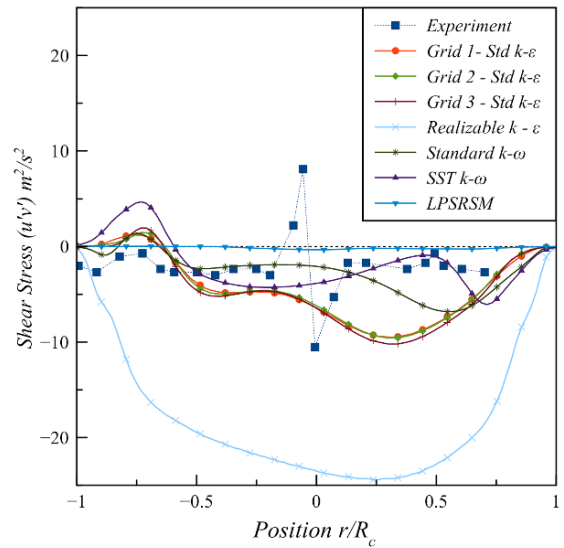
(a) Axial Velocity



(b) Transverse Velocity



(c) Turbulent Kinetic Energy



(d) Shear Stress

Figure 4: Velocity and turbulence characteristics at axial position $z = 130$ on dilution holes plane at isothermal flow conditions.

$z = 50$ mm and the same can be said for the predicted shear stress as shown in Fig. 4(d).

Therefore, it can be inferred that grid independence is being approached. To, ensure maximum accuracy, the authors have chosen to use 'Grid 3' for further simulations and analysis.

6.2. Assessment of Turbulence Models

In this section, the various turbulence models (i.e., standard $k - \epsilon$, realizable $k - \epsilon$, standard $k - \omega$, SST $k - \omega$, and LPS-RSM) used in this work are assessed by comparing the present computational results using Grid 3 with experimental studies (Heitor and Whitelaw, 1986; Heitor, 1985) for their suitability in predicting the isothermal flow in a realistic can-type gas turbine combustor geometry (refer Fig. 1).

6.2.1. Standard $k - \epsilon$ model predictions

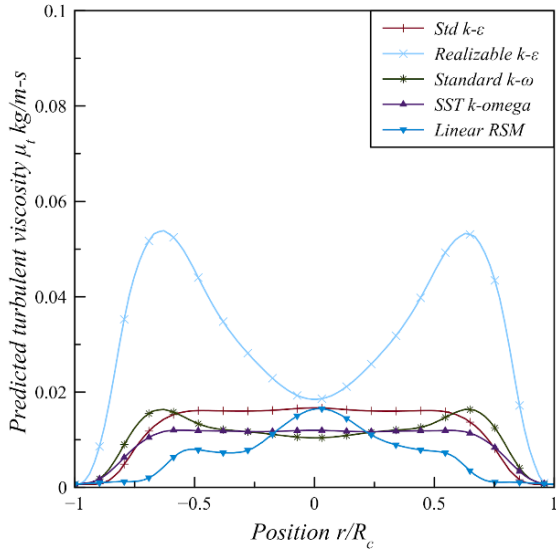
On comparing the predicted axial velocity profile using the standard $k - \epsilon$ model using grid 3 on the location $z = 50$ mm on the dilution holes plane in Fig. 3(a), it can be seen that the predicted axial velocity is not in the trend with the experimental measurement. The only position where it matches with the experimental values is at the radial position $r/R_c = -0.6$. The predicted axial velocity showing the non-negative axial velocity values indicates a lack of formulation present in the standard $k - \epsilon$ model to capture the central backflow which is represented in the experimental values in the radial position $r/R_c = -0.5$ to 0.5 . The standard $k - \epsilon$ model is based on the assumption of local isotropy which means that the turbulence is the same in all the directions at a given point. This assumption fails to accurately capture the complex flow patterns and vortical structures associated with swirling flows. This also leads to inadequate representation of the turbulent transport processes, including redistribution of momentum and the formation of secondary flows. The consequence of it can be seen in Fig. 3(b) where transverse velocity is underpredicted which indicates a lack of swirl in the vortex using the standard $k - \epsilon$ model. The predicted transverse magnitude switches from positive to negative at the centre position $r/R_c = 0.0$ in Fig. 3(b) indicating the position of the vortex core. Corresponding to this, the eddy viscosity curve of the standard $k - \epsilon$ model in Fig. 5(a) shows flatness from positions $r/R_c = -0.75$ to $r/R_c = 0.75$ showing eddy viscosity not being sensitive to the flow characteristics of the present case.

On comparing the predicted turbulence kinetic energy using the standard $k - \epsilon$ model in Fig. 3(c) it can be noticed that turbulence is inaccurately predicted. The turbulence is not represented well using the model, in confined swirling flows, turbulence is concentrated and intensified due to the swirling motion and flow recirculation within the core which is observed in experimental values. Besides, higher values of turbulence kinetic energy are also experimentally recorded near the wall due to the swirl which is additionally fed by primary jets entering the combustor from primary holes. The oversimplistic isotropic assumption led to higher turbulence at the outer edge of the vortex core, symmetrically, predicted at the positions $r/R_c = -0.75$ and $r/R_c = 0.75$ which is predicted due to the swirl originating from the swirler and dilution jets, and lower values predicted at the core around $r^* = \pm 0.25$ $r^* = -0.25$ and $r^* = 0.25$ in Fig. 3(c).

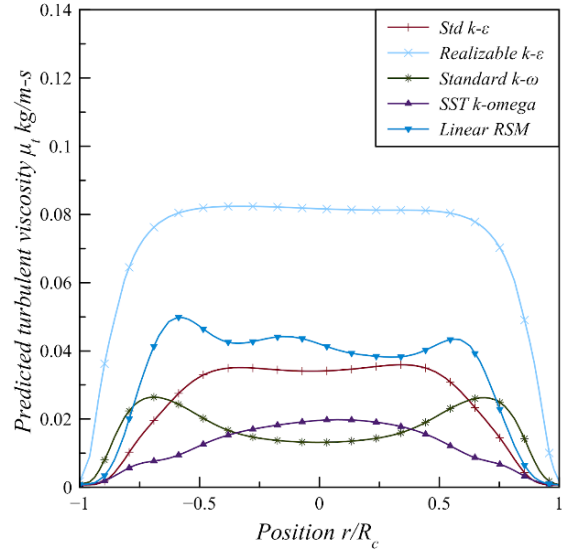
In the confined swirling flows, the shear stress is usually high due to the strong velocity gradients, especially at the vortex core which is observable in the experimental measurement around the position $r/R_c = 0.0$ in Fig. 3(d). Comparison with shear stress prediction using standard k-epsilon again indicates inaccuracy. The maximum shear stress values are obtained at the edge of the vortex at the positions $r/R_c = -0.75$ and $r/R_c = 0.75$ using the standard $k - \epsilon$ model, however, negligible values of shear stress are obtained at the centre position $r/R_c = 0.0$, again indicating the inability of the model to capture the flow dynamics of confined swirling flows inaccurately. The velocity vectors in Fig. 6(a) and streamlines of standard $k - \epsilon$ in Fig. 7(a) predictions also do not indicate flow reversal at the vortex core. The q-criterion shown in Fig. 8(a) also indicates that the vortex core progressively dilutes as the flow convects downstream towards dilution holes as mentioned above.

On observing the predicted axial velocity from standard k-epsilon simulation on dilution holes, in Fig. 4(a) the maximum velocity magnitude is predicted at central positions from $r/R_c = -0.25$ to $r/R_c = 0.25$. The predicted transverse velocity plot in Fig. 4(b) shows underprediction, the transverse velocity switches from positive to negative at the centre

Position $r/R_c = 0.0$ however, the underprediction points to the prediction of less swirl and also indicates that the vortex core diffuses as the flow convects downstream. The turbulence kinetic energy is overpredicted as shown in Fig. 4(c), which can be said to be due to the prediction of diffusion of the vortex core which enhances turbulence kinetic energy due to its mixing with the surrounding fluid. Still, the slightly higher prediction of turbulence kinetic energy close to the combustor wall could be attributed to additional turbulence produced due to the inlet of air inlets at dilution holes and its mixing with the surrounding fluid. While observing the experimental turbulence kinetic energy plot in the same figure, it can be seen that the maximum turbulence kinetic energy is recorded at the centre indicating the maximum fluctuations and thus steepest velocity gradients. The shear stress is also inaccurately predicted as shown in Fig. 4(d), the experimental values show the maximum magnitude of shear stress at the centre indicating the maximum magnitude of velocity gradients at the vortex core while shear stress is less pronounced and overall negative in the positions $r/R_c = -1.0$ to $r/R_c = -0.25$ and from $r/R_c = 0.25$ to $r/R_c = 1.0$. While the simulation results show a substantially larger magnitude of shear stress all over except at the centre indicating intensified mixing is predicted between the vortex and the surrounding fluid and with additional air entering the combustor through dilution holes, due to which higher and inaccurate turbulence kinetic energy is predicted at the same position, as above mentioned. The near eddy viscosity curve predicted on the dilution hole in Fig. 5(b) from positions $r/R_c = -0.5$ to $r/R_c = 0.5$ also indicates the model model assumes a uniform level of turbulence in this region regardless of the flow characteristics. This further substantiates a lack of sensitivity to the anisotropic nature of the swirling flows and the model's inability to accurately capture the dissipation of turbulence energy and corresponding changes in the flow dynamics accurately.



(a) at $z = 50$ mm on primary holes plane



(b) at $z = 130$ mm on dilution holes plane

Figure 5: Predicted turbulent viscosity at the axial position z on primary and dilution holes plane at isothermal flow conditions.

6.2.2. Realizable $k - \epsilon$ model predictions

On analysing the results obtained using the realizable $k - \epsilon$ model on the primary hole plane at $z = 50$ mm, the axial velocity prediction is not in trend with experimental values and is overpredicted. The predicted axial velocity, obtained from the realizable $k - \epsilon$ model, exhibits non-negative values, hence, like standard $k - \epsilon$ the realizable $k - \epsilon$ model has also failed to capture the central backflow observed in the experimental data within the radial position range of $r/R_c = -0.5$ to 0.5 . This observed discrepancy again suggests that the formulation of the realizable $k - \epsilon$ model cannot accurately predict the complexity of confined swirling flows. The transverse velocity is also inaccurately predicted as shown in Fig. 3(b). The predicted transverse velocity plot reveals an underprediction of the transverse velocity which suggests less swirl is predicted in the vortex. This observed discrepancy again suggests that the formulation of the realizable $k - \epsilon$ model cannot accurately predict the complexity of confined swirling flows.

The realizable $k - \epsilon$ model shares the same transport equation for turbulence kinetic energy as

the standard $k - \epsilon$ model while the transport equation of turbulent dissipation rate ϵ is derived using the transport equation of mean square of vorticity fluctuation (Tennekes and Lumley, 2018). The model is called realizable because it ensures the positivity of normal stress ($\overline{u'^2} > 0$) which by definition is a positive quantity and maintains the Schwarz inequality (refer Eq. 12). Schwarz inequality in the realizable $k - \epsilon$ model is used to bind the magnitude of shear stress in a fluid and to ensure that the stresses are realistic and physically meaningful. The turbulence velocity formulation remains isotropic. The realizability is achieved by modifying the formulation of C_μ which is no longer constant like the standard $k - \epsilon$ model (refer Eq. 13). This involves introducing additional terms and coefficients that depend on the strain rate and rotation rate (refer Eqs. 14 and 15) of the flows. These terms are aimed to assist in improving the turbulence-predicting ability of the model. However, it can be stated that these additional terms and model constants are not calibrated for the confined swirling flows, apart from isotropic eddy viscosity assumption and due to these reasons simulation results obtained are even less accurate than the standard $k - \epsilon$ model.

The underprediction of transverse velocity indicates less swirl and a weak vortex core also indicatesdemonstrates that the model is predictingpredicts a diffusion of vortex core even at the primary zone where experimental values indicate a very dominant swirl. The prediction of excessive diffusion of the vortex intensifies mixing with the surrounding fluid and leads to the development of regions of high-velocity gradients and significant turbulence at the region of vortex interaction with the surrounding fluid or at the vortex's outer edge (Davidson, 2015). This leads to the prediction of high turbulent kinetic energy at this region as seen in Fig. 3(c) in positions $r/R_c = -0.75$ to $r/R_c = 0.75$. This has also led to the prediction of high-magnitude shear stress in this area shown in Fig. 3(d).

The realizable $k - \epsilon$ relates turbulent viscosity with turbulent kinetic energy and the turbulent dissipation rate through a closure relationship (refer Eq. 9). The turbulent viscosity (μ_t , Eq. 9) is directly proportional to the square of turbulent kinetic energy (k) and inversely proportional to

the turbulent dissipation rate (ϵ). However, the model has predicted lower turbulent kinetic energy and shear stress at the vortex core or positions $r/R_c = -0.25$ to $r/R_c = 0.25$ as seen in Figs. 3(c) and 3(d). This is in contrast to the experimental data, which indicates high turbulent kinetic energy and shear stress at the vortex core. These discrepancies between the model's prediction and experimental data indicate that model's formulation is incapable of predicting the intricacies of confined swirling flow accurately. Correspondingly, the velocity vectors in (Fig. 6(b)) and streamlines in (Fig. 7(b)), and Q -criterion in (Fig. 8(b)) indicate a very small vortex core obtained using a realizable $k - \epsilon$ model.

The predicted mean axial and transverse velocity using the realizable $k - \epsilon$ model on the dilution hole plane ($z = 130$ mm) is not in trend with the experimental values and is overpredicted as seen in Figs. 4(a). The predicted transverse velocity using the same model is also not in trend with the experimental of the same as seen in Fig. 4(b). The predicted transverse velocity is positive throughout the plane, indicating no rotation and the vortex core originated upstream at the primary zone has completely diffused as the flow convected towards the dilution holes. The predicted axial and transverse velocity profiles exhibits characteristics more like a pipe flow than the he expected flow profile of the combustor flow near the dilution holes ($z = 130$ mm) plane.

On analysing the turbulent kinetic energy predictions by the realizable $k - \epsilon$ model in Fig. 4(c), it can be seen that turbulent kinetic energy is clearly overpredicted and completely not in trend with the experimental data. The higher value of turbulent kinetic energy is predicted near the wall in the proximity of dilution holes at positions $r/R_c = -0.75$ to $r/R_c = 0.75$ and the lower k values at positions $r/R_c = -0.25$ to $r/R_c = 0.25$. While experimental data suggest the maximum magnitude of turbulent kinetic energy at the centre of the plane, at positions $r/R_c = -0.25$ to $r/R_c = 0.25$. A comparison of turbulent kinetic energy prediction with other turbulence models indicates maximum turbulence is predicted using the realizable $k - \epsilon$ model. Relatively high overall turbulence is predicted using the realizable k-epsilon model because the

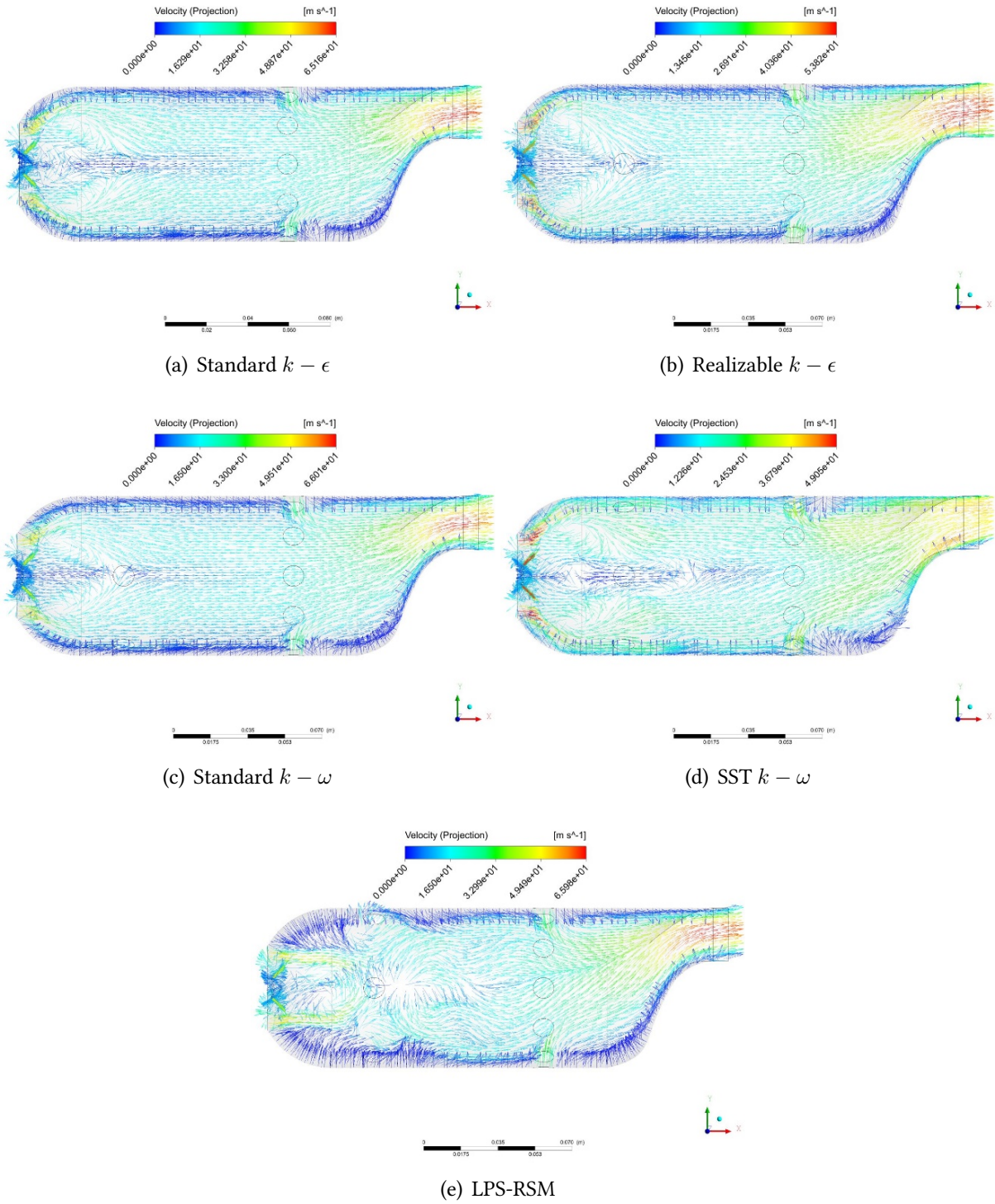


Figure 6: Comparison of velocity vectors predicted on X-Y plane using various turbulence models (a) Standard $k - \epsilon$ model, (b) Realizable $k - \epsilon$ model, (c) Standard $k - \omega$, (d) SST $k - \omega$, (e) LPS-RSM.

model predicted a rapid diffusion of the vortex core halfway before the fluid reached the dilution holes. This intensified mixing and interaction with the surrounding fluid and hence enhanced turbulence. Besides, the prediction of a higher value of turbulent kinetic energy values predicted near the wall at positions $r/R_c = -0.75$ to $r/R_c = 0.75$ can be due to additional air entering the combustor through dilution holes that can create flow gradients and vortical structures near the wall enhancing the turbulence energy in that region.

The shear stress prediction shown in Fig. 4(d) is also not in trend with the experimental values and is negative throughout the plane and very high overall values are predicted. The high negative shear stress predicted on the dilution hole plane can be attributed to the enhancement of turbulence due to vortex diffusion upstream and complex flow interactions and vortical structures present due to air entering the combustor liner through dilution holes. The turbulent viscosity profile of the realizable $k - \epsilon$ model in Fig. 5(b) shows considerably high magnitudes predicted with a nearly flat profile throughout the plane from position $r/R_c = -0.75$ to $r/R_c = 0.75$. The high magnitude of turbulent viscosity is predicted in the region of high turbulence in the realizable $k - \epsilon$ model due to model formulation. The nearly flat profile of the eddy viscosity suggests that the model assumes a relatively constant turbulent viscosity throughout the region, possibly due to the isotropic assumption of eddy viscosity. The present simulation shows the model's inability to simulate the anisotropic behaviour of confined swirling flows and complex interaction between the swirling flow, turbulence and energy transfer processes accurately as found in gas turbine combustors which have led to discrepancies between the predicted flows and observed flow characteristics.

6.2.3. Standard $k - \omega$ model predictions

In the axial velocity comparison between the predicted mean axial velocity using the standard $k - \omega$ model in Fig. 3(a), it can be observed that the predicted mean axial velocity is inaccurately predicted and not in trend with the measured values. The predicted axial velocity

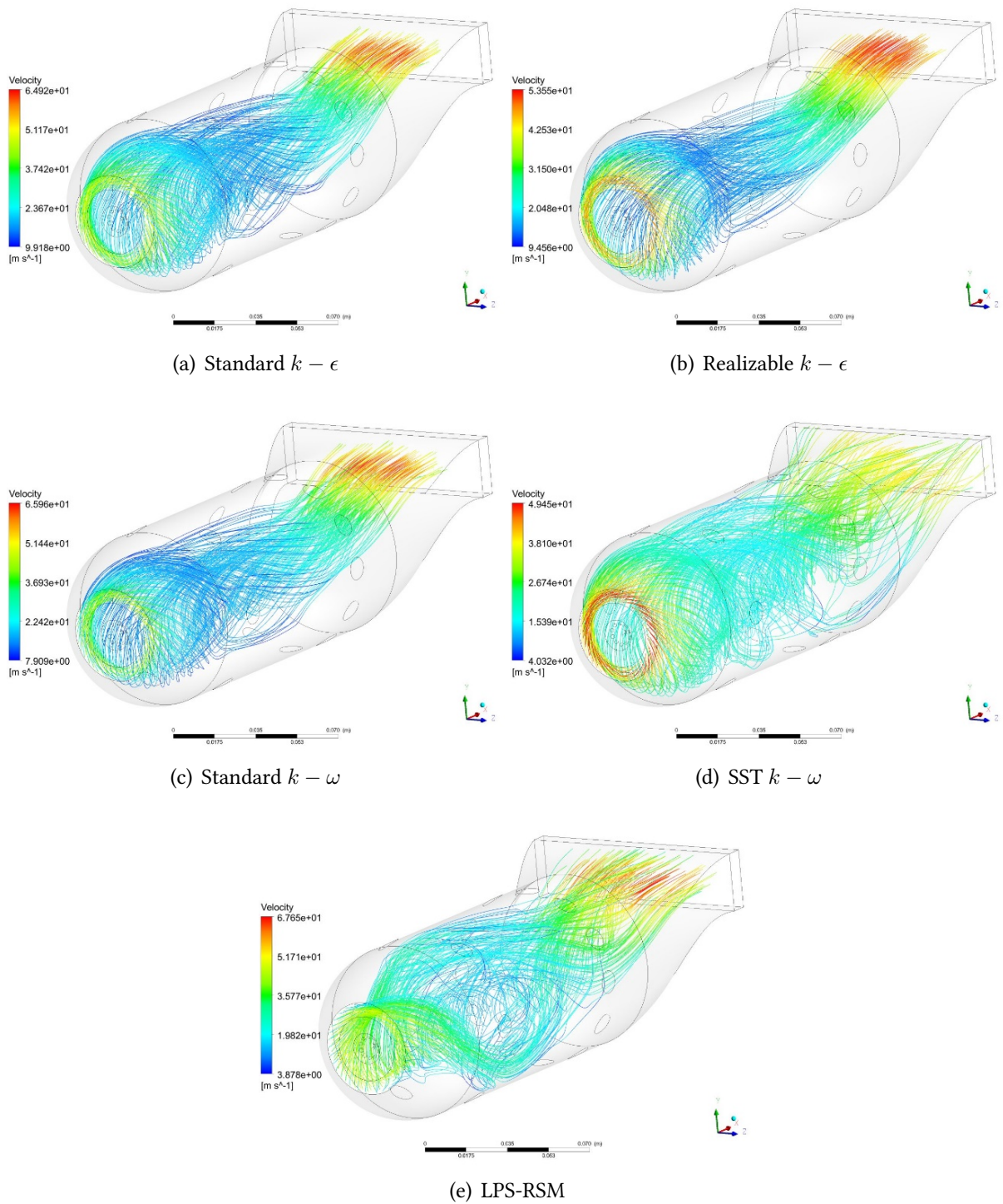


Figure 7: Comparison of velocity streamlines predicted using various turbulence models (a) standard $k - \epsilon$, (b) realizable $k - \epsilon$, (c) standard $k - \omega$, (d) SST $k - \omega$, (e) LPS-RSM.

again shows non-negative values indicating that the model has failed to predict the backflow present in the vortex flows. This can again be attributed to the assumption of isotropic turbulence in the standard $k - \omega$ model and the model formulation which may not fully capture the complex flow dynamics and mechanisms driving backflows in the vortex near primary holes of the combustor. The predicted mean transverse velocity in Fig. 3(b) is in trend with experimental values and is in fairly good agreement with the measured values. The position ($r^* = 0$) where the transverse velocity switches from positive to negative, $r/R_c = 0.0$ is also accurately predicted. The predicted turbulent kinetic energy is over-predicted and is not in agreement with the experimental values at the primary holes, as seen in Fig. 3(c). The maximum values are predicted near wall due to the swirling motion and are further enhanced by air entering from primary holes, whilst the minimum values are predicted at the center at the vortex core, where experimental values indicate maximum turbulence. This discrepancy as aforementioned can be attributed to the incapacities of the standard $k - \omega$ model has shown incapability to adequately capture the unique flow characteristic of flows in can combustors (confined swirling flows with additional primary and dilution jets), especially the interaction between the vortex core and primary jets.

The predicted magnitude of shear stress can also be said to be enhanced by the primary jets entering the combustor liner through primary holes. The experimental values also indicate the maximum same pattern, the predicted values are larger than experimental values and not aligned with them at both ends, positions $r/R_c = -0.75$ and $r/R_c = 0.75$. However, negligible shear stress is predicted at the centre position $r/R_c = 0.0$ or at the vortex core where maximum values of shear stress were experimentally recorded due to the development of backflow in the vortex core. The prediction of zero shear stress at the vortex core could be a limitation of the model to capture the flow physics adequately in that region.

On analysing the turbulence viscosity curve in Fig. 5(a) it can be said that the maximum turbulent viscosity is predicted near the combustor liner walls at the edge of the vortex due to

intense turbulent activity and shear effects in this region, further enhanced by air entering the combustor liner through primary holes. The turbulence viscosity represents the level of turbulence-induced mixing and momentum transfer in the flow, at the edge of the vortex, there are significant velocity gradients and strong vorticity, which results in enhanced turbulence and mixing. These conditions contributed to the generation of stronger turbulent eddies, contributing to the computation of higher turbulent viscosity in this region. On the other hand, with the flat profile of the turbulent viscosity at the centre of the vortex position $r/R_c = 0.0$ the computed velocity gradients and turbulence kinetic energy is lower, which has led to the flat profile.

On observing the standard $k - \omega$ model predictions on the dilution holes planes, the predicted axial velocity profile shown in Fig. 4(a) is not in trend with the experimental values, the maximum values are predicted at radial positions $r/R_c = -0.25$ and $r/R_c = 0.25$, while a slight trough can be seen at the centre of the plane at radial position $r/R_c = 0.0$. The transverse velocity shown in Fig. 4(b) is also underpredicted indicating model predicts diffusion of the vortex at the position which originated upstream at the primary zone by swirler. The diffusion of the vortex is also reflected in velocity vectors in Fig. 6(c), streamlines in Fig. 7(c), and Q -criterion in Fig. 8(c) as the fluid reaches the dilution holes plane.

The turbulent kinetic energy (k) is overpredicted, as seen in Fig. 4(c). The maximum values are obtained at the edge of the vortex close to the wall at radial positions $r/R_c = -0.75$ and $r/R_c = 0.75$, where velocity gradients are expected to be maximum, further enhanced by intensified mixing predicted between the vortex and the surrounding fluid due to vortex diffusion and additional air entering the combustor through dilution holes. The minimum values are predicted at the core of the vortex at radial positions $r/R_c = 0.0$, which contrasts with the experimentally maximum k is recorded at the position.

The maximum shear stress is also predicted at the edge of the vortex close to the wall at radial positions $r/R_c = -0.75$ and $r/R_c = 0.75$ where velocity gradients are expected to be high as

seen in Fig. 4(d). When the vortex diffuses, it undergoes deformation and spreads out in the flow field. This diffusion process can create regions of high-velocity gradients and enhanced shear stress at the edge of the vortex. The interaction between the turbulent flow, vortex and dilution jets, can lead to increased turbulent transport and mixing, resulting in elevated shear stress levels. However, the maximum shear stress is experimentally recorded at the centre position $r/R_c = 0.0$, presumably at the centre of the vortex core. The vortex core is characterized by high rotational velocities and strong velocity gradients. Interaction between the swirling flow and the surrounding liquid creates significant shear stress within the vortex structure (Dixon and Hall, 2014).

The underprediction of turbulent kinetic energy and shear stress in this region can be attributed to the inherent limitation of isotropic viscosity assumptions and simplifications in the standard $k - \omega$ model. The $k - \omega$ model is based on certain assumptions and empirical correlations that may not accurately capture the complex flow phenomenon accurately as in the present case. Fig. 5(b) shows that the maximum magnitude of the turbulent viscosity is predicted at the outer edge of the vortex core due to the complex flow behavior and velocity gradients in that region, shown in Fig. 5(b). In swirling flows, such as those found in vortex cores, there is a strong rotation of fluid particles around the central axis. This rotation leads to the development of high-velocity gradients and vorticity. At the outer edge of the vortex, where the flow is rapidly rotating, and the velocity gradients are highest, which contributes to the generation of turbulence and mixing of fluid elements, leading to an increased turbulent viscosity. As in the $k - \omega$ model, the specific dissipation rate (ω) equation (Eq. 17) includes a production term related to the mean flow strain rate. This term represents the transfer of kinetic energy from the mean flow strain rate to the turbulence, and it influences the turbulent viscosity. In regions of high strain rate or strong mean flow gradients, the production term (See section 4.2.3) can lead to higher values of ω and, consequently, higher turbulent viscosity. However, in the core region of a vortex, the mean flow strain rate is typically lower compared to the outer regions. This is

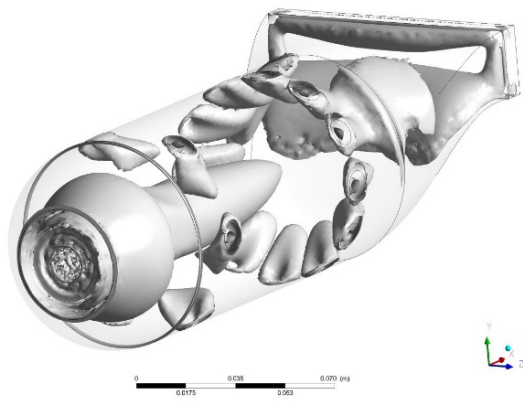
because the flow within the core is primarily characterized by rotation rather than deformation. This lower strain rate can result in a reduced production term and, consequently, a lower predicted turbulent viscosity. However, readers should note that turbulent viscosity is not a physical property but rather a modeling concept introduced by turbulence models to represent the complex nature of turbulence. It is typically introduced by turbulence models, such as RANS models, which provide closure equations to approximate the effects of turbulence on the flow.

6.2.4. SST $k - \omega$ model predictions

The axial velocity predicted on the primary hole plane using the SST $k - \omega$ model is also not accurate and also not in trend with the experimental measurement as seen in Fig. 3(a). However, amongst the two-equation turbulence models used in this work, only the SST $k - \omega$ model has been able to predict the negative axial velocity values in the vortex core region at radial positions $r/R_c = -0.25$ and $r/R_c = 0.25$ indicating that the model has managed to capture backflow found in complex vortex flows to some extent. The velocity vectors in Fig. 6(d) also reflect that the SST $k - \omega$ model predicts the presence of backflow in the vortex core.

The transverse velocity predictions are also inaccurate, and magnitudes are greater than the experimental measurements of the same, as can be seen in Fig. 3(b). The main reason for inaccuracy in the above prediction could be that SST $k - \omega$ is also based on isotropic turbulence. It is already established that turbulence in the confined swirling flow is anisotropic, leading to errors in the model prediction. Further, the SST $k - \omega$ model is also a linear eddy viscosity model, it assumes that turbulent viscosity is proportional to turbulent kinetic energy. This assumption is made to simplify the mathematical formulation of the model. However, it may not be suitable for the accurate prediction of confined swirling flows.

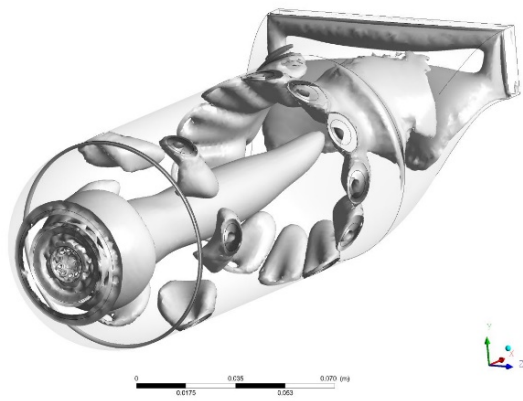
The predicted turbulence kinetic energy in Fig. 3(c) is also not in agreement with the experimental data and like other assessed two-equation models, it is also predicted maximum at the edge of the predicted vortex core at radial positions $r/R_c = -0.75$ and $r/R_c = 0.75$, close



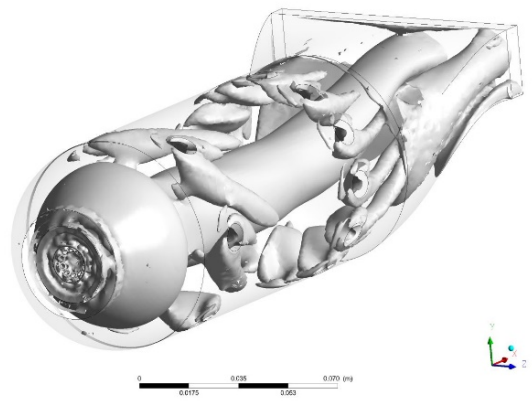
(a) Standard $k - \epsilon$



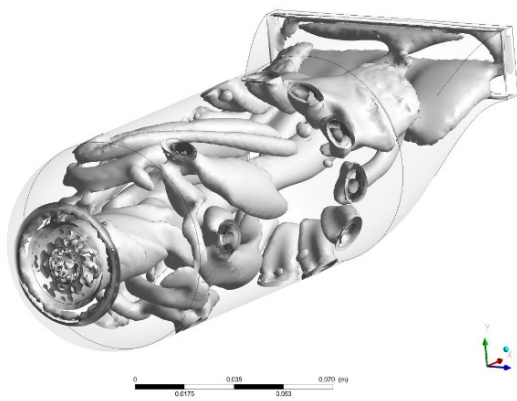
(b) Realizable $k - \epsilon$



(c) Standard $k - \omega$



(d) SST $k - \omega$



(e) LPS-RSM

Figure 8: Comparison of Q -criterion predicted using various turbulence models (a) standard $k - \epsilon$, (b) realizable $k - \epsilon$, (c) Standard $k - \omega$, (d) SST $k - \omega$, (e) LPS-RSM.

to the walls, and minimum magnitude is predicted at the vortex core at radial positions $r/R_c = -0.25$ and $r/R_c = 0.25$. Similarly, the maximum and minimum magnitudes of shear stress are predicted at $r^* = \pm 0.75$ and $r^* = \pm 0.25$, respectively, in Fig. 3(d). The maximum values occur at the vortex edge due to the most intense turbulence. The interaction of the primary jets with the surrounding fluid further enhances the turbulent intensity. It becomes strongest at the vortex, where shear forces and velocity gradients are most significant. The maximum magnitude of shear stress is also predicted in the same region at radial positions $r/R_c = -0.75$ and $r/R_c = 0.75$, and the minimum is predicted around the vortex core at radial positions $r/R_c = -0.25$ and $r/R_c = 0.25$. The lower level of turbulence predicted at the vortex core can be attributed to the model's inherent incapacities to accurately simulate confined swirling flows due to the model's assumption on which its formulation is based and the assumption of isotropic turbulence due to which the model may not fully capture the complexities of vortex flows in such confined environment.

On examining the predicted turbulent profile of the SST $k - \omega$ model in Fig. 5(a), it can be seen that the nearly flat profile predicted across the plane obtained indicates almost constant eddy viscosity. The predicted turbulent viscosity profile is similar to the standard $k - \epsilon$ model, however, is much lower in magnitude. This could be the reason why the vortex core is sustained till the combustor exit, as seen in the Q -criterion in Fig. 8(d) and velocity streamlines in Fig. 7(d). In the case of the SST $k - \omega$ model, the predicted lower μ_t may contribute to the sustained vortex structure. As the fluid moves within the vortex core, the lower μ_t facilitates the interaction between fluid layers with different velocities and vorticity, leading to a more coherent and stable vortex structure. On the other hand, in the standard $k - \epsilon$ model, where higher μ_t values are predicted, particularly at the core region, the vortex may be more prone to diffusion and dissipation. Nevertheless, both models failed to fully capture the anisotropic nature of the turbulence at the vortex core region.

When comparing the predicted mean axial velocity using the SST $k - \omega$ model with the

experimental measurements at the dilution holes plane in Fig. 4(a), it becomes evident that the mean axial velocity, like other evaluated two-equation models, does not exhibit a trend consistent with the experimental values. It is, however, noteworthy that the predicted mean axial velocity, although overpredicted, is relatively closer to the experimental values compared to the other evaluated two-equation models.

The predicted mean transverse velocity shown in Fig. 4(b), while still inaccurate, shows better agreement with other assessed two-equation turbulence models. The higher magnitude of the transverse velocity, exceeding that of other evaluated two-equation models, suggests a stronger swirl component and supports the observation of a sustained vortex core as discussed earlier. The above-mentioned disparities in predicted mean axial and transverse velocity with other assessed two-equation turbulence models could be attributed to the difference in the formulation of turbulent viscosity in the SST $k - \omega$ model. The SST $k - \omega$ model employs a different approach to estimate turbulent viscosity, taking into account the effects of the turbulent kinetic energy and the specific dissipation rate and additional formulation. This formulation may lead to variations in the predicted flow characteristics when compared to other turbulence models such as other evaluated two-equation models (see Eq. 27).

When observing the turbulent kinetic energy on the dilution hole plane in Fig. 4(c), it can be seen that lower kinetic energy is predicted throughout the plane than using the other two-equation models. Maximum values are still predicted at the vortex edge on the dilution holes plane at radial positions $r/R_c = -0.75$ and $r/R_c = 0.75$ using the SST $k - \omega$ model as a result of the complex flow dynamics in that region and minimum values are predicted at the centre of the dilution holes plane from radial positions $r/R_c = -0.25$ to $r/R_c = 0.25$. As aforementioned, the vortex core edge is characterized by strong velocity gradients and intense turbulence due to the swirling motion of the flow. These factors contribute to the higher turbulent kinetic energy levels near the vortex core edge and are further enhanced by the interaction of dilution jets with the convecting fluid which leads to an increase in mixing and

turbulence level. However, at most of the plain, at the positions $r/R_c = -0.5$ to $r/R_c = 0.5$, a nearly flat profile of turbulent kinetic energy is predicted, Further, the model failed to predict the peak at the center of the plane or the center of the vortex core, as observed in the experimental measurement. These observed discrepancies can be due to the model's inherent inability of the model to accurately simulate confined swirling flows accurately owing to model formulations including isotropic turbulence assumption. On observing the predicted shear stress in Fig. 4(d), the maximum shear stress is predicted at the vortex core edge due to the aforementioned intense velocity gradients and flow deformation in this region further enhanced by the interaction of dilution jets with swirling flows. The model has predicted lower shear stress at the centre position $r/R_c = -0.5$ to $r/R_c = 0.5$, the reasons for these discrepancies are mentioned above.

The turbulent viscosity is computed as maximum around the center of the vortex core where the turbulent kinetic energy is lowest and minimum at the vortex edge, shown in Fig. 5(b). The turbulent viscosity is a measure of the resistance of the fluid to shearing. It is calculated from the turbulent kinetic energy and the specific dissipation rate in the SST $k - \omega$ model. The turbulent viscosity is calculated highest at the centre of the vortex core where the turbulent kinetic energy is computed lowest. This is because the turbulence is being dissipated and the fluid is less able to resist shearing. On comparing the computed turbulent viscosity using the SST $k - \omega$ model with a computed turbulent velocity of other two-equation models in Fig. 5(b), it can be seen turbulent viscosity magnitude computed at the dilution hole using the SST $k - \omega$ model is lower than the other assessed two-equation models. This discrepancy can be attributed to the different formulations and closure assumptions employed in each model. The SST $k - \omega$ model combines elements of the $k - \epsilon$ and the standard $k - \omega$ models and aims to provide improved to improve predictions in a wider range of flow conditions. However, the specific coefficients, turbulence closure assumptions, and treatment of turbulence production, dissipation, and length scales in the SST $k - \omega$ model can lead to variations in turbulent

viscosity predictions. Still, from the assessment it can be stated SST $k - \omega$ model demonstrated superior performance compared to the other evaluated two-equation models in the present flow conditions.

6.2.5. Linear Pressure Strain - Reynolds Stress Model (LPS-RSM) predictions

On observing the predictions using the LPS-RSM (Linear Pressure Strain Reynolds Stress Model), it can be seen in Fig. 3(a) that the mean axial velocity is overestimated, however, is in trend with the measured values. The model has managed to capture the negative values of the axial velocity in the highly turbulent vortex core region. In highly turbulent vortex core regions, as experimental data of the reference study suggest, the axial velocity typically becomes negative. This is because as the vortex core is rotating, the fluid is being forced to move in a circular motion. This results in complex velocity gradients and vorticity patterns. The LPS-RSM managed to capture the negative axial velocity in a highly turbulent vortex core region because it takes into account the anisotropy of turbulence. In the LPS-RSM, the pressure strain term (ϕ_{ij}) in LPS-RSM is decomposed into slow and rapid pressure strain terms along with the wall reflection term (Eq. 37). The slow pressure strain term ($\phi_{ij,1}$, Eq. 38) contains the Reynolds stress anisotropic tensor (Eq. 38), which is a measure of anisotropy. The term is proportional to the amount of anisotropy in the Reynolds stress tensor. The slow pressure strain tensor can be thought of as a measure of the tendency of the Reynolds Stress Tensor to relax back to isotropy. The anisotropic stress tensor is modelled as a linear function of the turbulent kinetic energy (k). This means that the slow pressure strain term is proportional to the amount of turbulent kinetic energy in the flow. As the turbulent kinetic energy increases, the slow pressure strain term also increases, which helps to promote isotropy in a turbulent flow. The slow pressure strain term works by transferring energy from the anisotropic eddies to the isotropic eddies through the action of pressure forces. This helps to restore the isotropy of the turbulent flow and reduces the problems associated with anisotropy. The pressure forces act

on the turbulent eddies, they tend to equalize the stresses in the turbulent flow. Hence, pressure forces tend to shrink the anisotropic eddies. The rapid pressure strain term ($\phi_{ij,2}$, Eq. 39) is a measure of the interaction between the pressure and the velocity gradients. The rapid pressure strain term is responsible for the rapid distortion of turbulence, by transferring energy from the mean flow to the Reynolds stresses. It is an anisotropic term, despite being a symmetric tensor, since the different components of the pressure-strain tensor are not equal. In particular, the rapid pressure-strain term is larger when the mean strain rate tensor term (\bar{S}_{ij} , Eq. 3) is aligned with the direction of the Reynolds stresses. It can do this more effectively when the mean stress rate is aligned with the direction of the Reynold stress. The LPS-RSM often overestimates the velocity which is mainly due to the LPS-RSM assuming that the pressure-strain correlation is linear in the Reynolds stresses which means that the pressure strain correlation is proportional to the root mean square (RMS) of the Reynolds stresses.

The pressure strain correlation is a complex phenomenon, and it is not fully understood, however, it plays an important part and turbulence modelling. It is mostly understood as a term in the Reynolds stress transport equation that describes how the pressure field interacts with the Reynolds stresses. The pressure-strain correlation can be quadratic or even higher order in complex flows. The Linear Pressure correlation aligns the pressure field with the strain rate, this alignment creates a coupling between the pressure field and the velocity field which increases the momentum transfer between different layers of fluid. This causes an increase in turbulent viscosity and can also lead to an overestimation of the velocity of the fluid (Pope, 2000; Biswas and Eswaran, 2002; Kajishima and Taira, 2017; Bernard, 2018).

Hence, due to the above-mentioned reasons the transverse velocity, turbulent kinetic energy, and shear stress in the primary hole plane are overestimated (see Figs. 3(b)-3(d)) are overestimated on the primary hole plane. However, these results are in trend with the experimental data. The predicted turbulent viscosity profile using the LPS-RSM in Fig. 5(a) is similar to the predicted turbulent kinetic energy in Fig. 3(c) because the turbulent viscosity is

proportional to the square of the turbulent kinetic energy (see Eq. 9), in LPS-RSM, similar to the standard $k - \epsilon$ model. Due to consideration of anisotropy and model formulation, the model predicted the swirling more accurately than the two-equation models, hence, it can be seen in Figs. 6(e), 7(e) and 8(e) that the model managed to preserve the swirling vortex core is preserved till the combustor exit comparatively better than the two-equation counterparts.

The predicted axial velocity using LPS-RSM at the dilution holes plane shows an undulated profile in Fig. 4(a), the axial velocity is overpredicted, however, the waviness predicted shows that predictions are more in trend with the experimental data than the other assessed two-equation models. This is likely because the LPS-RSM model takes into account anisotropy as aforementioned. The transverse velocity is also more accurately predicted using the LPS-RSM than other assessed two-equation models as shown in Fig. 4(b), the predicted transverse velocity profile indicates the vortex core as it switches from positive to negative at almost the same position and is similar magnitude overall to the experimental data.

The turbulent kinetic energy is underpredicted but overall more accurate using the LPS-RSM model than two-equation models, however, is predicted flat at the centre of the plane. The turbulent kinetic energy is underpredicted with a flat profile at the center of the dilution holes plane using LPS-RSM in Fig. 4(c). However, it is overall more accurate than two-equation models. However, the experimental data and LPS-RSM prediction of transverse velocity show that the center of the vortex core lies on the center of the dilution holes plane centre. The centre of the vortex is a more chaotic region of the flow, with strong vortices and significant fluctuations which is indicated by the experimental data of turbulent kinetic energy in Fig. 4(c) as it shows a peak on this position. Hence, it can be stated that the linear pressure strain correlation in the LPS-RSM model, modelas underestimated the energy transfer of energy between different components of Reynolds stresses, hence, the model has failed to predict turbulence inaccurately at the vortex core on the dilution holes plane. On observing the predicted shear stress on the dilution hole plane, the predicted profile obtained using LPS-RSM

is also flat and shows negligible shear stress in Fig. 4(d), the reasons for which are mentioned above. The predicted turbulent viscosity has undulated profile and is relatively high compared to the other two-equation models except for Realizable $k - \epsilon$. Similar to the axial velocity profile in Fig. 4(a), the turbulent viscosity profile in Fig. 5(b) is undulated and relatively higher compared to the other two-equation, except for realizable $k - \epsilon$, models. The relatively higher turbulent viscosity indicates a prediction of a lower turbulence dissipation rate at this position. Despite these shortcomings, the authors would like to state that the predictions using the LPS-RSM predictions are still more accurate than the assessed two-equation models. The overall findings can be summarized as follows:

- The isotropic turbulence assumption of the standard $k - \epsilon$ model, which assumed equal turbulence in all directions at a given point, fails to accurately represent the turbulent transport processes and vortical structures. As a result, the model does not accurately capture the flow characteristics and complexities of confined swirling flows. Hence, axial velocity, transverse velocity, turbulence kinetic energy and shear stress are inaccurately predicted at both primary hole and dilution hole planes. The model failed to capture the flow reversal at the centre of the vortex and secondary flow features. The model also failed to capture the concentration and intensification of turbulence due to the swirling motion and flow recirculation due to which aforementioned turbulence kinetic energy is inaccurately predicted. The q -criterion and the underpredicted velocity profile at the dilution hole clearly showed that the vortex core progressively dilutes as the flow convects downstream towards the dilution holes, which is not in agreement with the experimental observations.
- The axial velocity predicted using the realizable $k - \epsilon$ model was overpredicted and not in agreement with experimental values at both primary and dilution holes planes, and also was non-negative at the centre of the primary hole plane, similar to the standard k-epsilon

model, indicating the model's inability to capture the central backflow as observed in the experimental data. The transverse velocity is also highly underpredicted at both positions, indicating a very weak swirl immediate diffusion of the vortex core as it begins to form compared to the dominant swirl recorded in the experimental data. The turbulence kinetic energy was overpredicted, with the maximum magnitude at the edge of the vortex and near the wall and the minimum at the centre of both planes. This trend was predicted because the model was simulating vortex diffusion which was also confirmed by the q -criterion which enhanced the turbulence due to intensified mixing between the vortex core and surrounding fluid, which also lead to inaccurate values of shear stress. The realizable k -epsilon turbulence is a modified form of the standard $k - \epsilon$ model, changes have been made to ensure that the model remains physical such as preserving the positivity of normal stress and maintaining the Schwarz inequality. However, the model has not been attuned to confined swirling flows, leading to less accurate predictions than the standard model. The model also incorporates additional terms and coefficients to improve turbulence prediction, but its isotropic formulation and lack of calibration limit its accuracy for confined swirling flows.

- The standard $k - \omega$ model failed to accurately predict axial velocity profiles and backflow in the vortex at the primary hole plane, while the transverse velocity was captured reasonably well, while the axial velocity was captured inaccurately and overpredicted at the dilution hole plane and transverse velocity was underpredicted particularly at the dilution holes plane, indicating vortex diffusion at this position, which was not observed in the experimental measurement. The predicted turbulent kinetic energy is overpredicted, with maximum values near the vortex edge close to the wall. This can be explained due to predicted intensified mixing between the vortex and the surrounding fluid due to vortex diffusion which was also noticed in q -criterion and additional air entering the combustor through dilution holes. On the contrary, the minimum values of

turbulent kinetic energy are predicted at the vortex core, opposing experimental observations. The model also predicted maximum shear stress at the edge of the vortex close to the wall, consistent with high-velocity gradients in that region. However, the predicted shear stress at the vortex core, where maximum values were experimentally recorded due to backflow development, was negligible at both primary and dilution hole planes. The isotropic turbulent viscosity assumptions and lack of a mechanism in the model to capture the intricacies of vortex flow and its interaction with surrounding fluid in confined swirling flows caused such discrepancies.

- The SST $k - \omega$ model does not accurately predict the axial velocity profiles on the primary hole plane, but it successfully captures the presence of backflow within the vortex core region. The transverse velocity predictions are also inaccurate but exhibit better agreement with other two-equation models. The axial velocity and transverse velocity predictions were inconsistent with the experimental measurement on the dilution hole plane, however, were better among the assessed two-equation models. The transverse velocity predictions and q -criterion indicated that the vortex core remained at the dilution holes plane and continued to the combustor exit as the flow convected towards it, which was consistent with the experimental observations. The model overpredicts turbulent kinetic energy, particularly at the vortex edge, and underpredicts it at the vortex core, opposing experimental observations at both positions. The predicted shear stress is highest at the vortex core edge due to intense velocity gradients, while negligible shear stress is predicted at the vortex core itself, which is again inconsistent with the experimental data at both primary and dilution hole planes. The SST $k - \omega$ model also assumes turbulence is isotropic, and the turbulent confined swirling flow is highly anisotropic, hence, discrepancies with experimental measurements are predicted. The SST $k - \omega$ model employs a different approach to estimate turbulent viscosity, taking into account the effects of the turbulent kinetic energy and the specific dissipation rate

with the additional formulation. This may have led to variations in the predicted flow characteristics when compared to other turbulence models such as other evaluated two-equation models.

- The LPS-RSM model overpredicted the mean axial velocity at the primary hole plane but was able to capture the negative axial velocity in the vortex core region, which is in agreement with experimental data. The model also overestimated the transverse velocity, turbulent kinetic energy, and shear stress on the primary hole plane. However, these results were in trend with the experimental data. This could be attributed to the model's consideration of turbulence anisotropy using the slow and rapid pressure strain terms in the pressure strain train terms. The overestimation of velocity and turbulence in the predictions can be attributed to the model's assumption of a linear pressure strain correlation which can be quadratic or even of higher order in complex flows. The mean axial velocity on the dilution holes was overestimated and exhibited an undulated profile. However, it was more in line with the experimental measurement than the other two-equation models. The transverse velocity was also more accurately predicted than the other assessed two-equation models. The turbulent kinetic energy was underpredicted but was also more accurately predicted than the two-equation models, however, inaccuracies were noticed particularly at the dilution holes plane where the model failed to capture the peak at the centre of the plane as found in the experimental measurement. The shear stress was predicted fairly accurately on the primary holes plane, however, on the dilution holes plane was underpredicted, the model failed to predict the peak at the centre of the plane as found in experimental data. Nevertheless, the q-criterion showed that the model has managed to preserve the swirling vortex core till the combustor exit as specified in experimental measurements. The noticed discrepancies between the experimental measurement and simulation results can be attributed to the Linear Pressure Strain Correlation in LPS-RSM, due to which the model

does take into account complexities of turbulence such as non-linear interaction between velocity gradients and hence the model has not been able to accurately simulate complexities related to swirling flows, vortex core and its interaction with the surrounding fluid. Nonetheless, as it accounts for anisotropy in turbulence, it still performed better than the two-equation models.

In summary, LPS-RSM generally performed better than the two-equation turbulence models due to anisotropic turbulence consideration. Considering non-linear pressure strain correlation can delineate the drawbacks and improve the accuracy of LPS-RSM for the computation of swirling turbulent flows.

7. CONCLUDING REMARKS

In this study, isothermal flow in the model can type combustor is simulated. The models assessed are standard $k - \epsilon$, realizable $k - \epsilon$, standard $k - \omega$, SST $k - \omega$ and LPS-RSM model. The predictive abilities of models are assessed by comparing the predicted axial velocity, transverse velocity, turbulent kinetic energy and shear stress at the primary hole and dilution hole planes. In this work, the predictive assessability of the turbulence models for isothermal flow in a combustor representing a constituent can combustor of the can-annular configuration used in jet engines has been performed using ANSYS Fluent based on the finite volume method. The RANS-based turbulence models assessed are the two-equation models (standard $k - \epsilon$, realizable $k - \epsilon$, standard $k - \omega$, SST $k - \omega$) and Linear Pressure Strain - Reynolds Stress Model (LPS-RSM). The prediction of the turbulence models for axial velocity, transverse velocity, turbulent kinetic energy, and shear stress have been compared with the experimental data at two different positions (i.e., the primary and dilution hole planes) in the combustor. The two-equation models have generally failed to predict both trends and accuracy of experimental results for the confined swirling flows at both positions, as the model formulations, assuming

isotropic turbulence, cannot capture the intricacies of vortex flow and its interaction with the surroundings in confined swirling flows. Amongst the two-equation models, the SST $k - \omega$ model yielded the most accurate, followed by standard $k - \omega$, realizable $k - \epsilon$, and standard $k - \epsilon$ models. Compared with two-equation models, LPS-RSM accounting for the anisotropic turbulence is promising for the confined swirling turbulent flow problems. While the LPS-RSM predictions have consistently captured the qualitative trends per experimental results, quantitatively, results are overestimated for all flow features, except for the turbulent kinetic energy and shear stress underestimated at the dilution holes plane. These observed discrepancies arise from the linear pressure-strain correlation in the LPS-RSM; this linear assumption is quite simplistic for complex flows. Hence, this study suggests that non-LPS-RSM or more advanced turbulence models can accurately predict the confined swirling flow in combustors.

DECLARATION OF COMPETING INTEREST

The authors declare that they have no known competing financial interests or personal relationships that could have appeared to influence the work reported in this paper.

REFERENCES

- R. A. Leyes, W. A. Fleming, [The History of North American Small Gas Turbine Aircraft Engines](#), American Institute of Aeronautics and Astronautics (AIAA), 1999.
- R. Royce, [The Jet Engine](#), Wiley, 5 edn., 2015.
- A. H. Lefebvre, D. R. Ballal, [Gas Turbine Combustion: Alternative Fuels and Emissions](#), CRC Press, 3 edn., 2010.
- W. G. Carter, The application of jet propulsion to military aircraft, [The Journal of the Royal Aeronautical Society](#) 50 (425) (1946) 347–358.
- K. Gradon, S. C. Miller, Combustion development on the Rolls-Royce spey engine, in: I. Smith (Ed.), [Combustion in Advanced Gas Turbine Systems](#), Pergamon, 45–76, 1968a.

- K. Gradon, S. C. Miller, Spey combustion - Development for military applications, in: [ASME 1968 Gas Turbine Conference and Products Show](#), vol. V001T01A021, American Society of Mechanical Engineers, 68-GT-21, 1968b.
- W. H. Hall, H. E. Chapman, Progress of the 727 jet in airline service, in: [SAE World Congress & Exhibition](#), SAE Technical Paper 640332, 1964.
- M. Heitor, J. Whitelaw, Velocity, temperature, and species characteristics of the flow in a gas-turbine combustor, [Combustion and Flame](#) 64 (1) (1986) 1–32.
- P. Koutmos, J. J. McGuirk, Isothermal flow in a gas turbine combustor – a benchmark experimental study, [Experiments in Fluids](#) 7 (5) (1989) 344–354.
- A. F. Bicen, J. J. McGuirk, J. M. L. M. Palma, Modelling gas turbine combustor flow fields in isothermal flow experiments, [Proceedings of the Institution of Mechanical Engineers, Part A: Journal of Power Engineering](#) 203 (2) (1989) 113–122.
- J. J. McGuirk, J. M. L. M. Palma, Experimental Investigation of the Flow Inside a Water Model of a Gas Turbine Combustor: Part 1—Mean and Turbulent Flowfield, [Journal of Fluids Engineering](#) 117 (3) (1995) 450–458.
- R. Srinivasan, H. C. Mongia, Numerical computations of swirling recirculating flow, Tech. Rep. NASA-CR-165196, AIRESEARCH-21-3517, NASA – Lewis Research Centre, 1980.
- G. J. Sturgess, S. A. Syed, Calculation of confined swirling flows, [International Journal of Turbo and Jet Engines](#) 7 (1–2) (1990) 103–121.
- D. G. Sloan, P. J. Smith, L. D. Smoot, Modeling of swirl in turbulent flow systems, [Progress in Energy and Combustion Science](#) 12 (3) (1986) 163–250.
- M. Nallasamy, Turbulence models and their applications to the prediction of internal flows: a review, [Computers & Fluids](#) 15 (2) (1987) 151–194.
- J. L. Xia, G. Yadigaroglu, Y. S. Liu, J. Schmidli, B. L. Smith, Numerical and experimental study of swirling flow in a model combustor, [International Journal of Heat and Mass Transfer](#) 41 (11) (1998) 1485–1497.
- P. Koutmos, J. J. McGuirk, Isothermal modeling of gas turbine combustors - Computational study, [Journal of Propulsion and Power](#) 7 (6) (1991) 1064–1071.
- J. J. McGuirk, J. M. L. M. Palma, The flow inside a model gas turbine combustor: calculations, [Journal of Engineering for Gas Turbines and Power](#) 115 (3) (1993) 594–602.
- W. P. Jones, A. Pascau, Calculation of confined swirling flows with a second moment closure, [Journal of Fluids Engineering](#) 111 (3) (1989) 248–255.
- R. Weber, B. M. Visser, F. Boysan, Assessment of turbulence modeling for engineering prediction of swirling vortices in the near burner zone, [International Journal of Heat and Fluid Flow](#) 11 (3) (1990) 225–235.

- Y. G. Lai, Predictive capabilities of turbulence models for a confined swirling flow, [AIAA Journal](#) 34 (8) (1996) 1743–1745.
- A. German, T. Mahmud, Modelling of non-premixed swirl burner flows using a Reynolds-stress turbulence closure, [Fuel](#) 84 (5) (2005) 583–594.
- A. M. Jawarneh, G. H. Vatistas, Reynolds stress model in the prediction of confined turbulent swirling flows, [Journal of Fluids Engineering](#) 128 (6) (2006) 1377–1382.
- W. P. Jones, S. Lyra, S. Navarro-Martinez, Large eddy simulation of turbulent confined highly swirling annular flows, [Flow, Turbulence and Combustion](#) 89 (3) (2012) 361–384.
- E. V. Palkin, M. Y. Hrebtov, D. A. Slastnaya, R. I. Mullyadzhyanov, L. Vervisch, D. K. Sharaborin, A. S. Lobasov, V. M. Dulin, Influence of a central jet on isothermal and reacting swirling flow in a model combustion chamber, [Energies](#) 15 (5) (2022) 1615.
- P. Wang, X. Wei, P. Shrotriya, W. Li, A. Ferrante, Investigation of isothermal flow inside a new combustor with two-stage axial swirler, [Journal of Applied Fluid Mechanics](#) 15 (2) (2022) 325–336.
- B. E. Launder, D. B. Spalding, [Lectures in Mathematical Models of Turbulence](#), Academic Press, 1972.
- T.-H. Shih, W. W. Liou, A. Shabbir, Z. Yang, J. Zhu, A new $\kappa - \epsilon$ eddy viscosity model for high Reynolds number turbulent flows, [Computers & Fluids](#) 24 (3) (1995) 227–238.
- D. C. Wilcox, [Turbulence Modeling for CFD](#), DCW Industries, La Canada, California, 2 edn., 1998.
- F. R. Menter, Two-equation eddy-viscosity turbulence models for engineering applications, [AIAA Journal](#) 32 (8) (1994) 1598–1605.
- M. M. Gibson, B. E. Launder, Ground effects on pressure fluctuations in the atmospheric boundary layer, [Journal of Fluid Mechanics](#) 86 (3) (1978) 491–511.
- S. Fu, B. E. Launder, M. A. Leschziner, Modelling strongly swirling recirculating jet flow with Reynolds-stress transport closures, in: [Symposium on Turbulent Shear Flows, 6th, Toulouse, France, Sept. 7-9](#), Proceedings (A88-38951 15-34). University Park, PA, Pennsylvania State University, 17–6–1 – 17–6–6, 1987.
- B. E. Launder, Second-moment closure and its use in modelling turbulent industrial flows, [International Journal for Numerical Methods in Fluids](#) 9 (8) (1989) 963–985.
- M. F. T. D. V. Heitor, [Experiments in Turbulent Reacting Flows](#), Ph.d. Thesis, Imperial College London, 1985.
- H. Versteeg, W. Malalasekera, [An Introduction to Computational Fluid Dynamics: The Finite Volume Method](#), Pearson Education (US), 2 edn., 2007.
- G. Alfonsi, Reynolds-Averaged Navier-Stokes Equations for Turbulence Modeling, [Applied Mechanics Reviews](#) 62 (4) (2009) 040802.

- H. Tennekes, J. L. Lumley, [A First Course in Turbulence](#), MIT Press, 2018.
- F. S. Lien, M. A. Leschziner, Assessment of turbulence-transport models including non-linear rng eddy-viscosity formulation and second-moment closure for flow over a backward-facing step, [Computers & Fluids](#) 23 (8) (1994) 983–1004.
- A. Ghobadian, S. A. Vasquez, A general purpose implicit coupled algorithm for the solution of Eulerian multiphase transport equation, in: [Proceedings of the International Conference on Multiphase Flow, Leipzig, Germany. 9 – 13 July, 2007](#).
- S. Patankar, [Numerical Heat Transfer and Fluid Flow](#), CRC Press, 1 edn., 1980.
- M. S. Cellek, A. Pinarbasi, Investigations on performance and emission characteristics of an industrial low swirl burner while burning natural gas, methane, hydrogen-enriched natural gas and hydrogen as fuels, [International Journal of Hydrogen Energy](#) 43 (2) (2018) 1194–1207.
- J. J. McGuirk, J. M. L. M. Palma, The influence of numerical parameters in the calculation of gas turbine combustor flows, [Computer Methods in Applied Mechanics and Engineering](#) 96 (1) (1992) 65–92.
- D. S. Crocker, E. J. Fuller, C. E. Smith, Fuel Nozzle Aerodynamic Design Using CFD Analysis, [Journal of Engineering for Gas Turbines and Power](#) 119 (3) (1997) 527–534.
- W. Jones, Large Eddy Simulation of turbulent combustion processes, [Computer Physics Communications](#) 147 (1-2) (2002) 533–537.
- F. di Mare, W. Jones, K. Menzies, Large eddy simulation of a model gas turbine combustor, [Combustion and Flame](#) 137 (3) (2004) 278–294.
- J. C. Oefelein, Large eddy simulation of turbulent combustion processes in propulsion and power systems, [Progress in Aerospace Sciences](#) 42 (1) (2006) 2–37.
- D. Veynante, Large Eddy Simulations of Turbulent Combustion, in: [Notes on Numerical Fluid Mechanics and Multidisciplinary Design](#), Springer Berlin Heidelberg, 113–138, 2009.
- B. A. Kader, Temperature and concentration profiles in fully turbulent boundary layers, [International Journal of Heat and Mass Transfer](#) 24 (9) (1981) 1541–1544.
- I. B. Celik, U. Ghia, P. J. Roache, C. J. Freitas, H. Coleman, P. E. Raad, Procedure for Estimation and Reporting of Uncertainty Due to Discretization in CFD Applications, [Journal of Fluids Engineering](#) 130 (7) (2008) 078001.
- A. Kumar, [Investigation of in-nozzle flow characteristics of fuel injectors of IC engines](#), Ph. D. Thesis, City University of London, London, UK, 2017.
- A. Kumar, A. Ghobadian, J. Nouri, Numerical simulation and experimental validation of cavitating flow in a multi-hole diesel fuel injector, [International Journal of Engine Research](#) 23 (6) (2021a) 958–973.

- A. Kumar, J. Nouri, A. Ghobadian, Predictions of vortex flow in a diesel multi-hole injector using the RANS modelling approach, [Fluids](#) 6 (12) (2021b) 421.
- S. Tang, R. Antonia, L. Djenidi, Approach towards local isotropy in statistically stationary turbulent shear flows, [Journal of Fluid Mechanics](#) 952 (2022) A17.
- P. Davidson, [Turbulence: An Introduction for Scientists and Engineers](#), Oxford University Press, 2 edn., 2015.
- S. L. Dixon, C. A. Hall, [Fluid Mechanics and Thermodynamics of Turbomachinery](#), Elsevier, 7 edn., 2014.
- S. B. Pope, [Turbulent Flows](#), Cambridge University Press, 2000.
- G. Biswas, V. Eswaran, [Turbulent Flows: Fundamentals, Experiments and Modeling](#), CRC Press, 2002.
- T. Kajishima, K. Taira, [Computational Fluid Dynamics: Incompressible Turbulent Flows](#), Springer, 2017.
- P. S. Bernard, [Turbulent Fluid Flow](#), Wiley, 2018.